Chapter 6

Dynamic Response Analysis

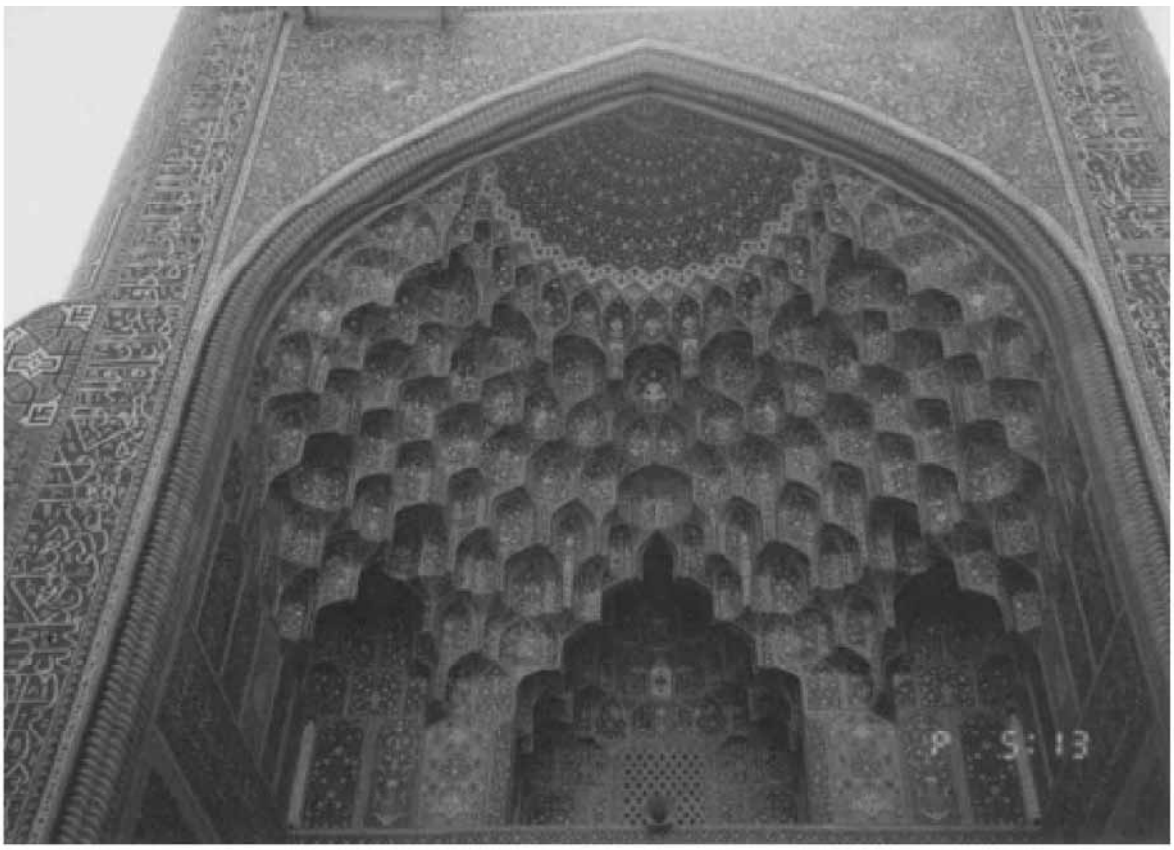

Masjid ye Imam, Isfahan, Iran.

Isfahan was a capital of the Safavid Dynasty of Iran since sixteenth Century. At the peak of its prosperity, this city was considered to be half of the world. The center of Isfahan was decorated by a beautiful garden and many marvellous buildings by monarchs of the dynasty mostly in the seventeenth Century. This city ended its time in 1722 upon invasion from north east.

Clay has a creep behavior; its deformation develops slowly with time under constant magnitude of stress. Therefore, the stress–strain curve of clay varies with the rate of loading. When loaded faster, clay reveals greater modulus and higher strength. These observation suggests that clay is a viscous material.

On the other hand, the stress–strain–strength characteristics of clay is controlled by a grain-to-grain friction and chemical bonding as well as electric interaction. The magnitude of these forces are not much dependent of the rate of loading. Consequently, the stress–strain behavior of clay is partially rate-dependent but partially rate-independent.

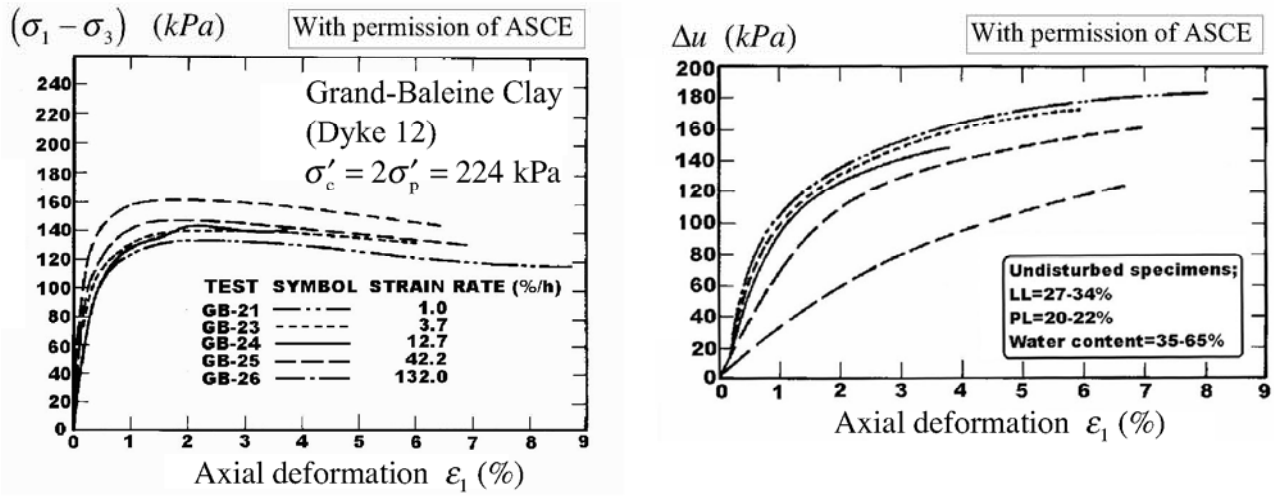

Fig. 6.1 Stress–strain and pore-water pressure behavior of normally consolidated Grande-Baleinee Clay (Lefebvre and LeBoeuf, 1987)

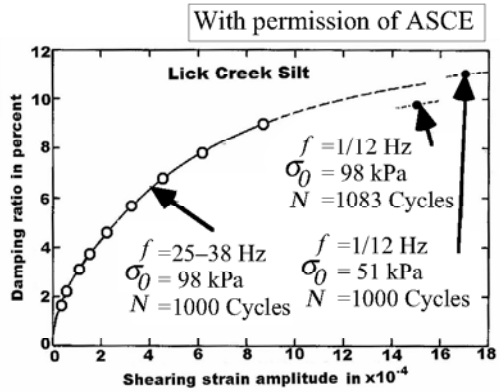

Fig. 6.2 Effect of frequency on damping ratio of silt (Hardin and Drnevich, 1972)

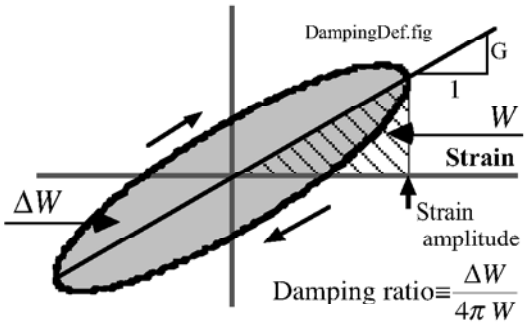

Fig. 6.3 Definition of damping ratio in soil dynamics

Figure 6.1 demonstrates undrained triaxial compression of clay with the axial strain rate varying between 1.0 %/hour and 132 %/hour. Evidently, the faster loading is associated with the greater strength and the less development of excess pore water pressure (the greater effective stress). In spite of the 132 times faster rate of loading, the maximum shear stress (strength) increased by about 25% only. The modulus increased by more or less the same amount as well. Thus, clay behavior is rate dependent to a limited extent.

Figure 6.2 illustrates a classic report on the damping ratio of Lick Creek Silt (liquid limit LL =22–34%, plasticity limit PL= 20–27%). Damping ratio stands for the amount of energy loss in cycle due to a hysteretic nature of the loop (Fig. 6.3). A viscous material has a proportionality between damping ratio and the rate of loading (frequency in Hz unit). Damping ratio has been known to increase as the amplitude of strain becomes larger. In Fig. 6.2, however, the relationship between damping ratio and the strain amplitude is independent of different frequencies of 25–38 and 1/12 Hz.

6.2 Significance of Complex Analysis

It may sound strange that many, although not all, dynamic analyses of ground make use of complex numbers: real and imaginary parts. Structural dynamics hardly do this. This practice has a reason in the simplicity in analysis and a use of complex-modulus modeling.

A discussion is initiated with a conventional single-degree-of-freedom model with mass, spring, and dashpot, which is called a Voigt model (Fig. 6.4a). The Voigt model can sustain a static force, while the other one in Fig. 6.4b (Maxwell model) cannot. Thus, the former model seems more similar to the real soil behavior.

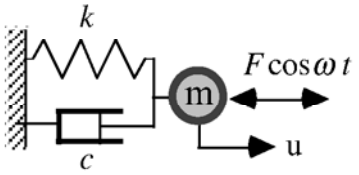

(a) Voigt model

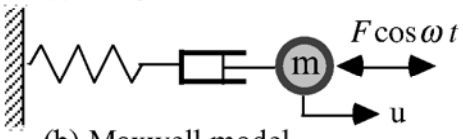

(b) Maxwell model

Fig. 6.4 Single-degree-of freedom models with real numbers

When a Voigt model is excited by a harmonic force of $F\cos\omega t$, the equation of motion is given by

$$m\frac{\mathrm{d}^2u}{\mathrm{d}t^2}+c\frac{\mathrm{d}u}{\mathrm{d}t}+ku=F\cos\omega t. \qquad (6.1)$$

Since the force is harmonic, the solution is assumed to be harmonic as well

$$u=A\sin\omega t+B\cos\omega t, \qquad (6.2)$$

where A and B are unknown parameters. By substituting (6.2) in (6.1) and equating the coefficients of sin and cos terms,

$$\begin{cases}(k-m\omega^2)A-c\omega B=0\\ c\omega A+(k-m\omega^2)B=F\end{cases},$$

which is then easily solved;

$$\begin{Bmatrix}A\\B\end{Bmatrix}=\frac{F}{(k-m\omega^2)^2+(c\omega)^2}\begin{Bmatrix}c\omega\\k-m\omega^2\end{Bmatrix}. \qquad (6.3)$$

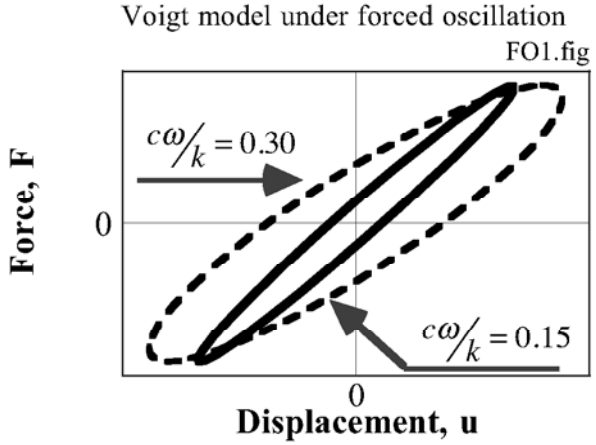

Fig. 6.5 Rate effects in force-displacement relationship of Voigt model subjected to forced oscillation

What follows employs a complex expression of force

$$m\frac{\mathrm{d}^2u}{\mathrm{d}t^2}+c\frac{\mathrm{d}u}{\mathrm{d}t}+ku=F\exp(\mathrm{i}\omega t). \qquad (6.4)$$

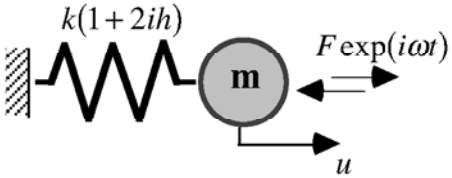

Fig. 6.6 Model of complex modulus

Equations (6.1) and (6.4) are equivalent when real parts of forces are compared. By assuming $u=U\exp(\mathrm{i}\omega t)$ in (6.4),

$$(-m\omega^2+ic\omega+k)U=F$$

$$U=\frac{F}{(k-m\omega^2)+ic\omega}=\frac{F\{(k-m\omega^2)-ic\omega\}}{(k-m\omega^2)^2+(c\omega)^2}.$$

By taking the real part of the solution $U\exp(\mathrm{i}\omega t)$,

$$\mathrm{Re}(u)=\frac{F\{(k-m\omega^2)\cos\omega t+c\omega\sin\omega t\}}{(k-m\omega^2)^2+(c\omega)^2}=A\sin\omega t+B\cos\omega t, \qquad (6.5)$$

which is identical with (6.3). Thus, analyses with real and complex numbers are equivalent when real parts of complex numbers are used. However, the derivation of (6.5) is simpler.

The force–displacement relationship of a Voigt model thus derived is illustrated in Fig. 6.5. It is evident that the size of the loop, which stands for the energy loss per cycle, increases as the loading frequency is made higher. Note that real soil does not exhibit such rate dependency (Fig. 6.2 and Sect. 10.9).

The frequency independency of damping ratio (Sect. 6.1) can also be achieved by changing the dashpot parameter with the loading frequency (inverse proportionality: $\propto 1/\mathit{frequency}$). This idea, however, is not acceptable from a mathematical viewpoint. When the input consists of harmonic motion of different frequencies, the equation of motion is given by

$$m\frac{\mathrm{d}^2u}{\mathrm{d}t^2}+c\frac{\mathrm{d}u}{\mathrm{d}t}+ku=\sum_j\left(a_j\ \sin\omega t+b_j\ \cos\omega t\right). \tag{6.6}$$

It is then expected to derive the solution by superimposing individual solutions for respective frequency components

$$u(t)=\sum_j\left(A_j\ \sin\omega t+B_j\ \cos\omega t\right). \tag{6.7}$$

The practice of superposition is justified only when the given differential equation is linear. When the c value varies with ω, however, the equation is not linear any more and, from the mathematical viewpoints, the superposition as (6.7) is not reasonable anymore. In other words, the earthquake response is irregular and its frequency varies with time in a random manner. Hence, it is difficult to determine any single number of c parameter. An alternative method of analysis is either a complex-modulus model (Sect. 9.1) or the use of nonlinear stress–strain model (e.g., hyperbolic stress–strain model in Sect. 11.1 or elastoplasticity in Sect. 11.3).

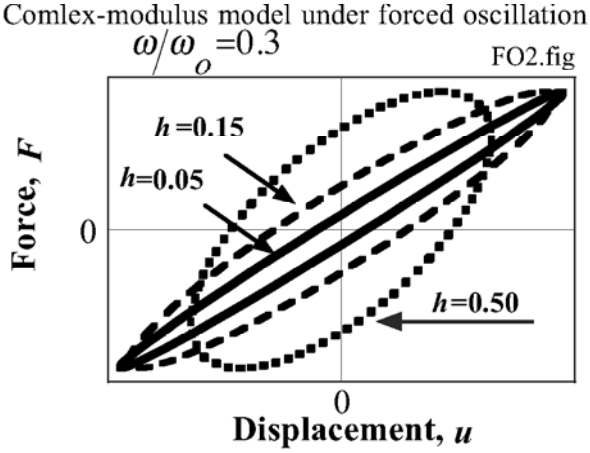

Fig. 6.7 Effects of h parameter on force-displacement loop of complex-modulus model

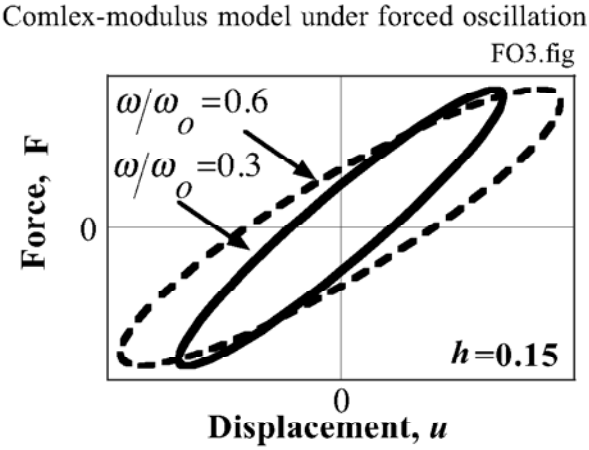

Fig. 6.8 Loading rate effects on force–displacement loop of complex-modulus model

The Voigt model is often replaced in earthquake geotechnical engineering by a complex-modulus model in which a spring parameter has an imaginary part (Fig. 6.6). As will be discussed later in Sect. 9.2, this imaginary part stands for an energy dissipation, eliminating the use of a rate-dependent dashpot in the model (Fig. 6.5). The equation of motion is

$$m\frac{\mathrm{d}^2u}{\mathrm{d}t^2}+k(1+2\mathrm{i}h)u=F\exp(\mathrm{i}\omega t). \tag{6.8}$$

By assuming $u=U\exp(\mathrm{i}\omega t)$ again,

$$U=\frac{F\{(k-m\omega^2)-2ikh\}}{(k-m\omega^2)^2+4k^2h^2}\quad\text{and}\quad \mathrm{Re}(u)=\frac{F\left\{\left(k-m\omega^2\right)\cos\omega t+2kh\,\sin\omega t\right\}}{\left(k-m\omega^2\right)^2+4k^2h^2}. \tag{6.9}$$

The energy dissipation in a complex-modulus model is governed by the "*h*" parameter. Figure 6.7 demonstrates that the greater *h* value makes the loop bigger and increases the energy loss per cycle. In addition to this, Figure 6.8 reveals the effects of loading frequency. While the amplitude of displacement varies with the frequency, the damping ratio (Fig. 6.3) is not affected. This feature matches the nature of soil.

Transient response is a response starting from a state of stationary condition: *displacement= velocity= 0.* The amplification during transient motion is different from what was obtained for a steady-state response in Sect. 6.2. A simple analysis is made in this section of a transient response of a rate-dependent single-degree-of-freedom model in Fig. 6.9. The equation of motion in terms of the relative displacement "*u*" is given by

$$\frac{\mathrm{d}^2u}{\mathrm{d}t^2} + 2h\omega_0\frac{\mathrm{d}u}{\mathrm{d}t} + \omega_0{}^2u = -\exp(\mathrm{i}\omega t) \tag{6.10}$$

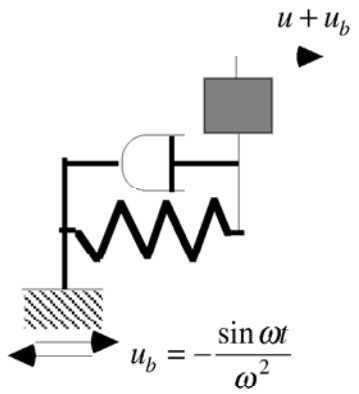

Fig. 6.9 Transient response of a simple model to harmonic shaking

Note that the base acceleration of $\sin\omega t$ is replaced by $\exp(i\omega t)$ for simplicity of calculation. Hence, the imaginary part of a complex solution to be derived will be adopted. By using the initial condition of $u=\mathrm{d}u/\mathrm{d}t=0$ at time = 0, a complex solution is given by

$$\frac{\mathrm{d}^2(u+u_b)}{\mathrm{d}t^2} = -\frac{(\lambda_1+\lambda_2)i\omega - \lambda_1\lambda_2}{(\lambda_1 - i\omega)(\lambda_2 - i\omega)}\exp(\mathrm{i}\omega t)$$
$$-\frac{1}{\lambda_1-\lambda_2}\left\{\frac{\lambda_1{}^2\exp(\lambda_1 t)}{\lambda_1 - i\omega} - \frac{\lambda_2{}^2\exp(\lambda_2 t)}{\lambda_2 - i\omega}\right\}$$
$$\text{for} \quad h<1 \tag{6.11}$$

where $\begin{Bmatrix}\lambda_1\\ \lambda_2\end{Bmatrix} = \left(-h \pm i\sqrt{1-h^2}\right)\omega_o$, ω_0=natural circular frequency, and h the critical damping ratio.

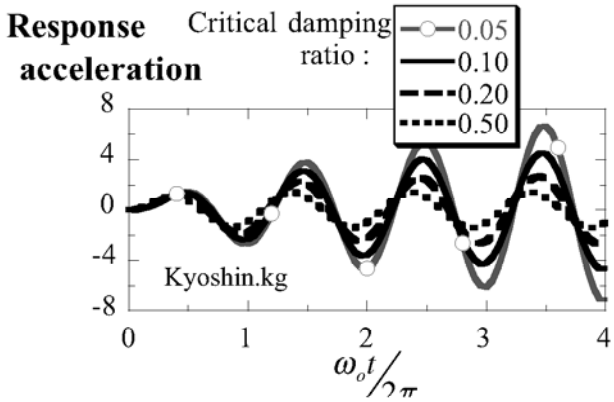

Fig. 6.10 Transient acceleration response to resonant input shaking

Figure 6.10 indicates the time history of response acceleration for a resonant input ($\omega = \omega_0$), varying with the critical damping ratio. For a unit amplitude of input acceleration, the response acceleration does not immediately reach the steady-state amplitude of $1/(2h)$; it takes a longer time for smaller critical damping ratio.

The electric power industries (変電所等における電気設備の耐震対策指針) have been employing such a resonant motion (only 2 or 3 cycles) for seismic design of transformers (変圧器), switches (開閉装置), etc. in place of real earthquake acceleration time histories. Figure 6.11 shows that the amplification of acceleration derived from 2 cycles (共振正弦2波) or 3 cycles (共振正弦3波) of harmonic resonant motion is comparative to those calculated for an irregular earthquake motion.

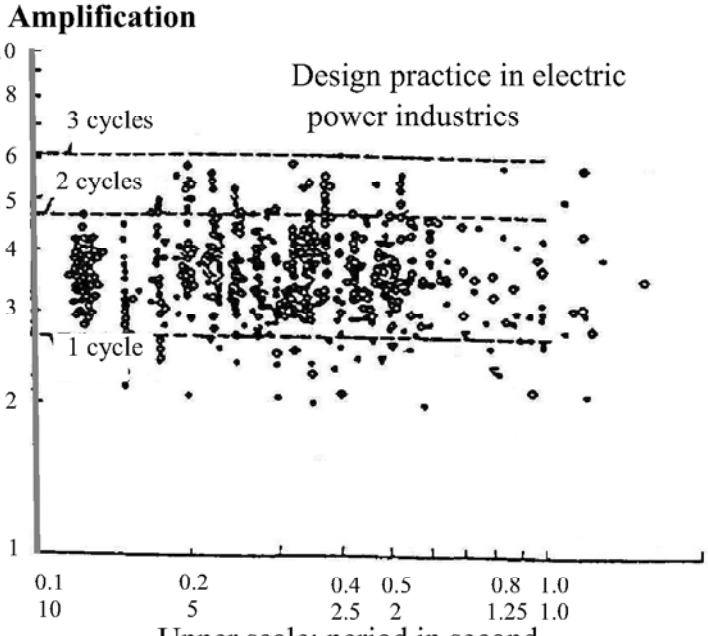

Fig. 6.11 Acceleration amplification for harmonic and irregular input motions (critical damping ratio = 0.05) (Japan Electric Association, 1998).

Among two kinds of techniques of dynamic response analyses, the conventional analyses in soil dynamics have been conducted in the frequency domain (Sect. 4.4). The major features and shortcomings of the frequency-domain analyses are summarized below.

- The equation of motion,

$$m\frac{\mathrm{d}^2u}{\mathrm{d}t^2}+k(1+2\mathrm{i}h)u=f\exp(\mathrm{i}\omega t)$$

in Sect. 9.4 is solved by assuming a harmonic response of $u=U\exp(\mathrm{i}\omega t)$. Load amplitude, f, and material properties do not change with time (steady state response).
- Calculation of time history of shaking as well as the maximum acceleration and velocity is widely conducted by frequency-domain analyses.
- Response to irregular loading is calculated by summing up harmonic (sinusoidal) responses under different frequencies (theory of Fourier series expansion in Sect. 9.11), see Fig. 6.12.
- Since laboratory tests on behavior of soils under cyclic loading have been conducted by applying harmonic stress cycles to soil specimens, test results on nonlinear soil properties such as $G/G_{\max}$ and damping ratio versus strain amplitude, can be directly used in the response analyses.
- Since the steady-state response analysis cannot take into account the variation of properties with time, degradation (softening) of clay and liquefaction of sand after excess pore water development are out of scope.
- Since the response is assumed to be harmonic, it comes back to the initial condition. Hence, residual deformation that remains after earthquake loading cannot be predicted.

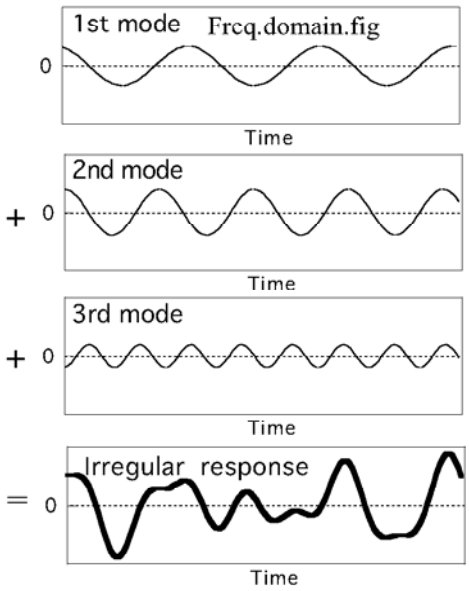

Fig. 6.12 Irregular response as summation of component harmonic modes

On the other hand, time-domain analyses directly integrates the equation of motion of

$$m\frac{\mathrm{d}^2u}{\mathrm{d}t^2}+r\left(u,\frac{\mathrm{d}u}{\mathrm{d}t}\right)=f(t)$$

in which $r(u, \mathrm{d}u/\mathrm{d}t)$ stands for the nonlinearly developed stress in soil, see Fig. 6.13. One of the famous techniques for direct integration is Newmark β method, see Sect. 6.6. Features of the time-domain analyses are described below.

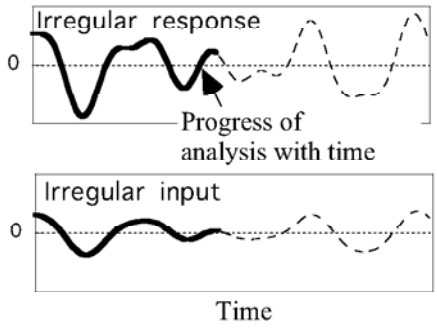

Fig. 6.13 Principle of time-domain analysis

- The nonlinearity of soil, $r(u,\mathrm{d}u/\mathrm{d}t)$, is often modeled by elasto-plastic models. Being theoretically beautiful, those models require detailed laboratory tests on undisturbed soil samples.
- Previous test results on $\mathrm{G}/G_{\max}$ and damping ratio are not enough to determine parameters in elasto–plastic models.
- Irregularity of input motion does not make any computational problem.
- It is possible to take into account the change of soil properties with time.
- Residual deformation can be automatically calculated, although its accuracy is not clear.
- Development of excess pore water pressure and consequent liquefaction can be handled only by the time-domain analysis (Sect. 22.3).
- Hence, demands for time-domain analyses are increasing today.

It is concluded, therefore, that the choice of the type of analyses depends upon what kind of calculation is being planned; e.g., time domain analysis suits studies on the development of excess pore water pressure, consequent softening of soil, and residual deformation. The frequency domain analysis is good at the assessment of maximum acceleration for example.

6.5 Numerical Integration of Equation of Motion in The Time Domain

Integration of equation of motion in the time domain is advantageous over the one in the frequency domain in that it can easily take into account the nonlinearity of material properties as well as the irregular time history of external load (transient analysis). On the other hand, being numerical, it cannot exhibit clearly the general scope of a concerned dynamic phenomenon, namely, the parameter effects. Moreover, nonlinearity of soil properties have been experimentally studied so far by using constant amplitudes of stress or strain. This situation directly fits an analysis on harmonic shaking. Therefore, most dynamic analysis of ground to date uses the idea of harmonic shaking. The irregularity of shaking is considered by using the theory of Fourier series (equivalent linear method in Sect. 9.10). It will be possible in future that a simple and useful plasticity theory is developed and becomes widely available.

This page illustrates a simple example of direct integration in the time domain. An example is taken of a simple equation of motion with a single-degree-of-freedom

$$m\frac{\mathrm{d}^2u}{\mathrm{d}t^2}+c\frac{\mathrm{d}u}{\mathrm{d}t}+ku=R(t), \tag{6.12}$$

in which u stands for the displacement, $\mathrm{d}u/\mathrm{d}t$ and $\mathrm{d}^2u/\mathrm{d}t^2$ the velocity and acceleration, respectively, and R(t) the external load that changes with time. It is assumed that the response is already known up to time T, while the response at $T+\Delta t$ after a short time increment of Δt is going to be calculated.

All the numerical techniques for solution of (6.12) requires some assumption about time change of response. One of the assumptions is that the acceleration varies linearly with time within a short increment of Δt

$$\frac{\mathrm{d}^2u(t)}{\mathrm{d}t^2}=\frac{\mathrm{d}^2u(T)}{\mathrm{d}t^2}+\frac{\dfrac{\mathrm{d}^2u(T+\Delta t)}{dt^2}-\dfrac{\mathrm{d}^2u(T)}{\mathrm{d}t^2}}{\Delta t}(t-T), \tag{6.13}$$

where $\mathrm{d}^2u(T)/\mathrm{d}t^2$ is the known acceleration at T, while $\mathrm{d}^2u(T+\Delta t)/\mathrm{d}t^2$ is the unknown acceleration at $T+\Delta t$. By integrating (6.13) with time,

$$\begin{aligned}
\frac{\mathrm{d}u(T+\Delta t)}{\mathrm{d}t}&=\frac{\mathrm{d}u(T)}{\mathrm{d}t}+\frac{\mathrm{d}^2u(T)}{\mathrm{d}t^2}\Delta t+\frac{1}{2}\left\{\frac{\mathrm{d}^2u(T+\Delta t)}{dt^2}-\frac{\mathrm{d}^2u(T)}{dt^2}\right\}\Delta t\\
&=\frac{\mathrm{d}u(T)}{\mathrm{d}t}+\frac{1}{2}\left\{\frac{\mathrm{d}^2u(T+\Delta t)}{\mathrm{d}t^2}+\frac{\mathrm{d}^2u(T)}{\mathrm{d}t^2}\right\}\Delta t \qquad (6.14)\\
u(T+\Delta t)&=u(T)+\frac{\mathrm{d}u(T)}{\mathrm{d}t}\Delta t+\frac{1}{2}\frac{\mathrm{d}^2u(T)}{\mathrm{d}t^2}\Delta t^2+\frac{1}{6}\left\{\frac{\mathrm{d}^2u(T+\Delta t)}{dt^2}-\frac{\mathrm{d}^2u(T)}{dt^2}\right\}\Delta t^2\\
&=u(T)+\frac{\mathrm{d}u(T)}{\mathrm{d}t}\Delta t+\Delta t^2\left\{\frac{1}{6}\frac{\mathrm{d}^2u(T+\Delta t)}{dt^2}+\frac{1}{3}\frac{\mathrm{d}^2u(T)}{dt^2}\right\}\Delta t^2
\end{aligned}$$

Substituting (6.14) in the equation of motion (6.12) at $T+\Delta t$,

$$\left(m+\frac{\Delta t}{2}c+\frac{\Delta t^2}{6}k\right)\frac{\mathrm{d}^2u(T+\Delta t)}{\mathrm{d}t^2}=R(T+\Delta t)-c\left\{\frac{\mathrm{d}u(T)}{\mathrm{d}t}+\frac{\Delta t}{2}\frac{\mathrm{d}^2u(T)}{\mathrm{d}t^2}\right\}$$

$$-k\left\{u(T)+\Delta t\frac{\mathrm{d}u(T)}{\mathrm{d}t}+\frac{\Delta t^2}{3}\frac{\mathrm{d}u^2(T)}{\mathrm{d}t^2}\right\} \tag{6.15}$$

$$\frac{\mathrm{d}^2u(T+\Delta t)}{\mathrm{d}t^2}=\frac{R(T+\Delta t)-c\left\{\dfrac{\mathrm{d}u(T)}{\mathrm{d}t}+\dfrac{\Delta t}{2}\dfrac{\mathrm{d}^2u(T)}{\mathrm{d}t^2}\right\}-k\left\{u_T+\Delta t\dfrac{\mathrm{d}u(T)}{\mathrm{d}t}+\dfrac{\Delta t^2}{3}\dfrac{\mathrm{d}^2u(T)}{\mathrm{d}t^2}\right\}}{\left(m+\dfrac{\Delta t}{2}c+\dfrac{\Delta t^2}{6}k\right)}. \tag{6.16}$$

Thus, the acceleration at $T+\Delta t$ is obtained. By substituting it in (6.14), the velocity and displacement are obtained as well. Then, the calculation proceeds towards the next time increment.

Unfortunately, the numerical method as described above is nothing more than being conceptual. When the time increment is greater than a certain fraction of the natural period of (6.12), the calculated response erroneously grows without limit. This nature is called “conditionally stable.” The author prefers some other methods that are unconditionally stable. For example, see Sects. 6.6 and 9.8.

Newmark proposed a popular method for direct integration of equation of motion

$$m\frac{\mathrm{d}^2u}{\mathrm{d}t^2}+c\frac{\mathrm{d}u}{\mathrm{d}t}+ku=R(t). \tag{6.17}$$

Newmark employed the following relationships

$$\frac{\mathrm{d}u(T+\Delta t)}{\mathrm{d}t}=\frac{\mathrm{d}u(T)}{\mathrm{d}t}+\left\{(1-\gamma)\frac{\mathrm{d}^2u(T)}{\mathrm{d}t^2}+\gamma\frac{\mathrm{d}^2u(T+\Delta t)}{\mathrm{d}t^2}\right\}\Delta t$$

$$u(T+\Delta t)=u(T)+\frac{\mathrm{d}u(T)}{\mathrm{d}t}\Delta t+\left\{\left(\frac{1}{2}-\beta\right)\frac{\mathrm{d}^2u(T)}{\mathrm{d}t^2}+\beta\frac{\mathrm{d}^2u(T+\Delta t)}{\mathrm{d}t^2}\right\}\Delta t^2. \tag{6.18}$$

By comparing (6.18) with (6.14), it is found that a combination of $\beta=1/6$ and $\gamma=1/2$ represents a linear variation of acceleration within a short time increment. Certainly, other combinations stand for different variation of acceleration with time. By substituting (6.18) in (6.17),

$$\left(m+\gamma\Delta tc+\beta\Delta t^2k\right)\frac{\mathrm{d}^2u(T+\Delta t)}{\mathrm{d}t^2}=R(T+\Delta t)-c\left\{\frac{\mathrm{d}u(T)}{\mathrm{d}t}+\Delta t(1-\gamma)\frac{\mathrm{d}^2u(T)}{\mathrm{d}t^2}\right\}$$
$$-k\left\{u(T)+\Delta t\frac{\mathrm{d}u(T)}{\mathrm{d}t}+\Delta t^2\left(\frac{1}{2}-\beta\right)\frac{\mathrm{d}u^2(T)}{\mathrm{d}t^2}\right\}. \tag{6.19}$$

Thus, $\mathrm{d}^2u(T+\Delta t)/\mathrm{d}t^2$ is obtained. It is then substituted in (6.18) to calculate $\mathrm{d}u(T+\Delta t)/\mathrm{d}t$ and $u(T+\Delta t)$. The analysis then proceeds to the response at $T+2\Delta t$.

The author prefers to use a combination of $\beta=1/4$ and $\gamma=1/2$, which makes the analysis unconditionally stable (see Sect. 6.5). A constant acceleration of $\mathrm{d}^2u(t)/\mathrm{d}t^2=\left\{\mathrm{d}^2u(T)/\mathrm{d}t^2+\mathrm{d}^2u(T+\Delta t)/\mathrm{d}t^2\right\}/2$ is represented for by $\beta=1/4$, while $\gamma=1/2$ does not generate numerical damping. Figure 6.14 illustrates the calculated response for $c=0$ and $R=0$ with the initial condition of $u=1$, $\mathrm{d}u/\mathrm{d}t=0$, and $\mathrm{d}^2u/dt^2=k/m$. As compared with the rigorous solution of $u=\cos\left(\sqrt{k/m}\times t\right)$, $\gamma<0.5$ produces erroneous increase of amplitude, $\gamma=0.5$ successfully reproduces the response, and $\gamma>0.5$ makes decay of response. This decay is called numerical damping. Although the numerical damping is a kind of error, it is often used to erase erroneous impulse that is numerically generated when nonlinear response of structure is analyzed. For detailed mechanism of unconditional stability and numerical damping, refer to Sect. 9.8.

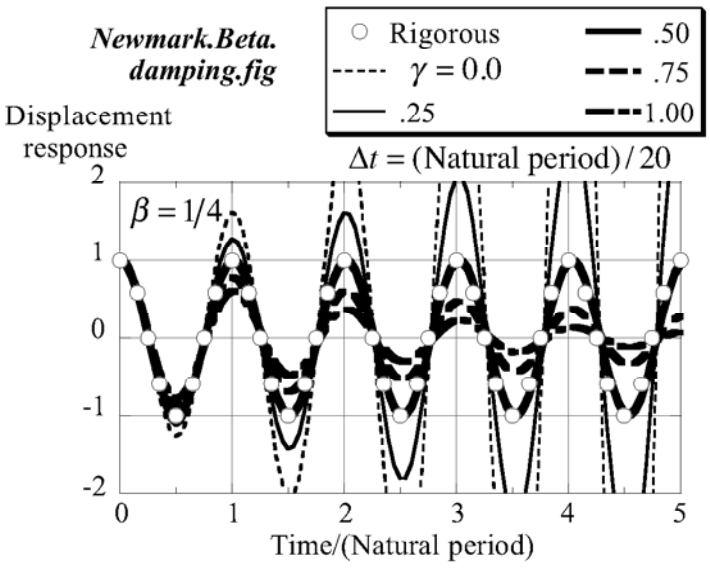

Fig. 6.14 Free vibration calculated by Newmark β method

It is certainly possible to solve the equation of motion in terms of displacement, in contrast

to the use of acceleration in (6.19), and then to calculate velocity and acceleration.

Newmark´s method is one of the direct integration methods for equation of motion. The following section addresses the mechanism of numerical damping and unconditional stability (Sect. 6.6) by applying the method to a simple undamped (viscosity = 0) equation of free vibration without damping

$$\frac{\mathrm{d}^2u}{\mathrm{d}t^2}+\omega_0{}^2u=0, \tag{6.20}$$

in which ω_0 stands for the natural circular frequency of this model.

The present calculation follows the original one made by Togawa (1975) with $\gamma=1/2$. In Newmark´s method, the variation of velocity and displacement over a short time interval of Δt is approximated by

$$\left(\frac{\mathrm{d}u}{\mathrm{d}t}\right)_{T+\Delta t}=\left(\frac{\mathrm{d}u}{\mathrm{d}t}\right)_T+\Delta t\left\{(1-\gamma)\left(\frac{\mathrm{d}^2u}{\mathrm{d}t^2}\right)_T+\gamma\left(\frac{\mathrm{d}^2u}{\mathrm{d}t^2}\right)_{T+\Delta t}\right\}$$
$$u_{T+\Delta t}=u_T+\Delta t\left(\frac{\mathrm{d}u}{\mathrm{d}t}\right)_T+\Delta t^2\left\{\left(\frac{1}{2}-\beta\right)\left(\frac{\mathrm{d}^2u}{\mathrm{d}t^2}\right)_T+\beta\left(\frac{\mathrm{d}^2u}{\mathrm{d}t^2}\right)_{T+\Delta t}\right\}. \tag{6.21}$$

By substituting (6.21) in (6.20),

$$\begin{bmatrix}1 & \omega_0{}^2\gamma\Delta t\\ 0 & 1+\omega_0{}^2\beta(\Delta t)^2\end{bmatrix}\begin{Bmatrix}\frac{\mathrm{d}u}{\mathrm{d}t}\\ u\end{Bmatrix}_{T+\Delta t}=\begin{bmatrix}1 & -\omega_0{}^2\gamma\Delta t\\ \Delta t & 1-\omega_0{}^2\left(\frac{1}{2}-\beta\right)(\Delta t)^2\end{bmatrix}\begin{Bmatrix}\frac{\mathrm{d}u}{\mathrm{d}t}\\ u\end{Bmatrix}_T. \tag{6.22}$$

By introducing an eigen value problem of this equation

$$\lambda\begin{bmatrix}1 & \omega_0{}^2\gamma\Delta t\\ 0 & 1+\omega_0{}^2\beta(\Delta t)^2\end{bmatrix}\begin{Bmatrix}\frac{\mathrm{d}u}{\mathrm{d}t}\\ u\end{Bmatrix}=\begin{bmatrix}1 & -\omega_0{}^2\gamma\Delta t\\ \Delta t & 1-\omega_0{}^2\left(\frac{1}{2}-\beta\right)(\Delta t)^2\end{bmatrix}\begin{Bmatrix}\frac{\mathrm{d}u}{\mathrm{d}t}\\ u\end{Bmatrix}, \tag{6.23}$$

in which the eigen value, λ, is complex. Note that

$$\left(\frac{\mathrm{d}u}{\mathrm{d}t}\right)_{T+\Delta t}=\lambda\left(\frac{\mathrm{d}u}{\mathrm{d}t}\right)_T \text{ and } u(T+\Delta t)=\lambda u(T) \tag{6.24}$$

are implied here in complex numbers. When the numerical calculation maintains stability (calculated response does not increase towards infinity, see Fig. 6.14), $|\lambda|\le 1$. When no numerical damping occurs, furthermore, $|\lambda|=1$. Thus, the eigen value has to be calculated. Because (6.23) has a nontrivial solution of $\vec{u}$ (not zero), the value of determinant is equal to zero

$$\begin{vmatrix}\lambda-1 & \omega_0{}^2\gamma\Delta t(\lambda+1)\\ -\Delta t & \lambda\left\{1+\omega_0{}^2\beta(\Delta t)^2\right\}-1+\omega_0{}^2\left(\frac{1}{2}-\beta\right)(\Delta t)^2\end{vmatrix}=0 \tag{6.25}$$

$$\lambda^2+\frac{-2+\omega_0{}^2(\Delta t)^2\left(\frac{1}{2}+\gamma-2\beta\right)}{1+\omega_0{}^2\beta(\Delta t)^2}\lambda+\frac{1+\omega_0{}^2\left(\beta+\gamma-\frac{1}{2}\right)(\Delta t)^2}{1+\omega_0{}^2\beta(\Delta t)^2}=0. \tag{6.26}$$

By denoting two solutions of λ by $\lambda=\lambda_1$ and $\lambda=\lambda_2$, which are either real or complex,

$$\lambda_1+\lambda_2=\frac{2-\omega_0{}^2(\Delta t)^2\left(\frac{1}{2}+\gamma-2\beta\right)}{1+\omega_0{}^2\beta(\Delta t)^2} \qquad \text{and}$$

$$\lambda_1\lambda_2=\frac{1+\omega_0{}^2\left(\beta+\gamma-\frac{1}{2}\right)(\Delta t)^2}{1+\omega_0{}^2\beta(\Delta t)^2}=1+\frac{\omega_0{}^2\left(\gamma-\frac{1}{2}\right)(\Delta t)^2}{1+\omega_0{}^2\beta(\Delta t)^2}. \tag{6.27}$$

The type of solutions, real or complex, depends on the sign (positive or negative) of

$$D=\left\{\frac{2-\omega_0{}^2(\Delta t)^2\left(\frac{1}{2}+\gamma-2\beta\right)}{1+\omega_0{}^2\beta(\Delta t)^2}\right\}^2-4\left\{\frac{1+\omega_0{}^2\left(\beta+\gamma-\frac{1}{2}\right)(\Delta t)^2}{1+\omega_0{}^2\beta(\Delta t)^2}\right\}$$

$$=\frac{\omega_0{}^2(\Delta t)^2}{1+\omega_0{}^2\beta(\Delta t)^2}\left[\omega_0{}^2(\Delta t)^2\left\{\left(\gamma+\frac{1}{2}\right)^2-8\beta\gamma\right\}-8\gamma\right]. \tag{6.28}$$

To achieve stability in analysis,

$$\text{both } |\lambda_1|\le 1 \text{ and } |\lambda_2|\le 1 \tag{6.29}$$

are needed.

Equation (6.27) is used to understand the mechanism of numerical damping.

(1) When $\gamma=1/2$, for example,

$$\lambda_1\lambda_2=1 \text{ and } D=\frac{\omega_0{}^2(\Delta t)^2}{1+\omega_0{}^2\beta(\Delta t)^2}\left\{\omega_0{}^2(\Delta t)^2(1-4\beta)-4\right\}.$$

It is implied by $\lambda_1\lambda_2=1$ that, if solutions of λ take two real and different numbers, one of them is greater than 1 and violates the requirement for stability (6.29). Hence, solutions of λ have to be real, equal to each other, or complex numbers. The requirement of $D\le 0$ leads to

$$\omega_0{}^2(\Delta t)^2(1-4\beta)\le 4.$$

Consequently, the dynamic analysis with $\gamma=1/2$ is

– Unconditionally stable when $\beta\ge 1/4$
– Stable when $\beta<1/4$ but $\Delta t\le 2\Big/\left(\omega_0\sqrt{1-4\beta}\right)$
– Unstable if $\beta<1/4$ and $\Delta t>2\Big/\left(\omega_0\sqrt{1-4\beta}\right)$

(2) When $\gamma<1/2$, (6.27) implies $\lambda_1\lambda_2<1$. The solution of the equation of motion decays with time when D in (6.28) is less than or equal to zero. This is called numerical damping.

An elementary analysis is made of a two-layered elastic horizontal deposit (Fig. 6.15). The surface layer is equivalent to an alluvium (沖積層), whilst the lower layer is an older deposit or sometimes a base rock. In reality, there is often a stiff gravelly layer at the bottom of alluvium with SPT-N (N値) > 40. The age of two layers is discontinuous (unconformity 不整合) due to geological history.

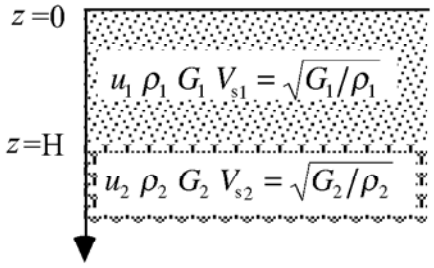

Fig. 6.15 Model of two-layered deposit

It is reasonable to assume a vertical propagation of S wave near the surface (see Fig. 4.7). With reference to Sect. 4.4, the equation of S-wave propagation is solved

$$\frac{\partial^2 u}{\partial t^2} = V_s^2 \frac{\partial^2 u}{\partial z^2}.$$

When a harmonic shaking is the case, the horizontal displacement, u, is derived as

$$u_1 = E_1 \exp\left\{i\omega\left(t + \frac{z}{V_{s1}}\right)\right\} + F_1 \exp\left\{i\omega\left(t - \frac{z}{V_{s1}}\right)\right\} \quad \text{in the top layer } (0 \le z \le H \text{ in Fig. 6.15})$$

$$u_2 = E_2 \exp\left\{i\omega\left(t + \frac{z-H}{V_{s2}}\right)\right\} + F_2 \exp\left\{i\omega\left(t - \frac{z-H}{V_{s2}}\right)\right\} \quad \text{in the base layer } (H \le z),$$

where E_1 to F_2 are constants. Note that the real parts of these solutions are used in practice. When this complex expression is not preferred, describe the solution as a sum of sin and cos functions. Shear stress is given by $\tau = G\partial u/\partial z = \rho V_s^2 \partial u/\partial z$,

$$\tau_1 = i\omega\rho_1 V_{s1}\left[E_1 \exp\left\{i\omega\left(t + \frac{z}{V_{s1}}\right)\right\} - F_1 \exp\left\{i\omega\left(t - \frac{z}{V_{s1}}\right)\right\}\right]$$

$$\tau_2 = i\omega\rho_2 V_{s2}\left[E_2 \exp\left\{i\omega\left(t + \frac{z-H}{V_{s2}}\right)\right\} - F_2 \exp\left\{i\omega\left(t - \frac{z-H}{V_{s2}}\right)\right\}\right].$$

Because the shear stress is zero at any t at the surface (z = 0), unless there is no structure, F_1=E_1. Moreover, both displacement and shear stress are continuous at the interface ($z = H$).

$$2E_1 \cos\frac{\omega H}{V_{s1}} = E_2 + F_2 \quad \text{and} \quad 2E_1 i\frac{\rho_1 V_{s1}}{\rho_2 V_{s2}} \sin\frac{\omega H}{V_{s1}} = E_2 - F_2.$$

Thus, all the constants are determined in terms of E_1.

$$\begin{Bmatrix} E_2 \\ F_2 \end{Bmatrix} = E_1\left(\cos\frac{\omega H}{V_{s1}} \pm i\frac{\rho_1 V_{s1}}{\rho_2 V_{s2}}\sin\frac{\omega H}{V_{s1}}\right)$$

- The amplitude of ground surface motion is $2E_1$.
- The free boundary condition at the surface (stress = 0) make the upward (E_1) and the downward (F_1 = E_1) propagations equal to each other in their intensity.
- The amplitude of upward propagation in the base rock is E_2. If the base rock is directly exposed to the air (rock outcrop), $2E_2$ is the surface motion. Hence, $2E_2$ is called the outcrop motion.
- E_2 is produced by the earthquake source and the travel path of the earthquake wave. It is the true input motion to the site of concern.
- The baserock motion of E_2+F_2 has F_2 which is the result of wave reflection at $z = H$ and $z = 0$. F_2 is

affected by the nature of the surface layer and therefore is not the true INPUT to the site.

– Therefore, E_2 has a more essential meaning than E_2+F_2.

The baserock here may not be a real rock. Being called “the engineering baserock,” in reality it is often a pleistocene soil (更新世、氷河期堆積物) or a soft rock.

The amplitude of motion in a horizontal layer, U_1, is given by

$$U_1 = |u_1| = 2E_1 \cos\frac{\omega z}{V_{s1}}.$$

The variation of U_1 with depth is illustrated in Fig. 6.16. U_1 is equal to E_2+F_2 at the baserock ($z = H$), and the ratio of U_1 at the surface and at the base is conventionally called the amplification in terms of $E + F$, denoted by Amp*(E + F)* below.

$$\mathrm{Amp}(E+F) = 1\Big/\cos\frac{\omega H}{V_{s1}}$$

This amplification is greater than or equal to 1 and takes an infinite value when $\omega H/V_{s1} = (n-1/2)\pi$ where n = 1,2,3,$\cdots$. The state of this infinite amplification is called *resonance*. Theoretically, the base amplitude is zero at resonance.

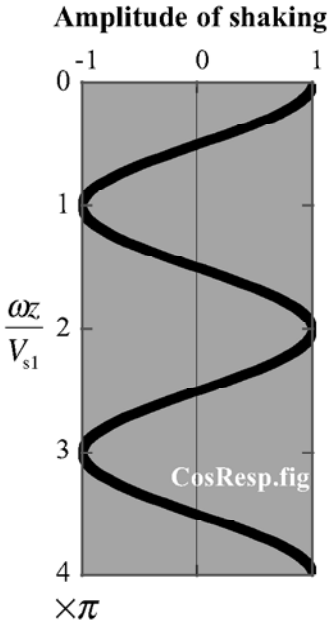

Fig. 6.16 Variation of amplitude with depth

At the fundamental mode of resonance (n = 1) with $\mathrm{Amp}(E+F) \to \infty$, the period of motion is obtained by

$$T = \frac{2\pi}{\omega} = \frac{4\pi H}{\pi V_{s1}} = \frac{4H}{V_{s1}}. \qquad (6.30)$$

This particular natural period is denoted by T_G which is the time that S wave needs to make 2 return trips between the surface and the base (21.4). See Table 21.2 for classification of subsoil by T_G.

Amp(E + F) does not directly indicate the ability of shaking amplification of the surface soil. To show this ability, it is more suitable to use the ratio of surface shaking and the input shaking signal. This goal is achieved by another definition of amplification factor in what follows.

Another type of amplification is defined by the ratio of surface motion to the true input motion E_2. It is denoted by Amp(2E) here as conventionally practiced.

$$\mathrm{Amp}(2E) = \left|\frac{2E_1}{2E_2}\right| = 1\Big/\left|\cos\frac{\omega H}{V_{s1}} + i\frac{\rho_1 V_{s1}}{\rho_2 V_{s2}}\sin\frac{\omega H}{V_{s1}}\right|$$

$$= 1\Big/\sqrt{\cos^2\frac{\omega H}{V_{s1}} + \left(\frac{\rho_1 V_{s1}}{\rho_2 V_{s2}}\sin\frac{\omega H}{V_{s1}}\right)^2} \qquad (6.31)$$

At resonance when $\omega H/V_{s1} = (n-1/2)\pi$,

$$\mathrm{Amp}(2E) = \frac{\rho_2 V_{s2}}{\rho_1 V_{s1}}. \qquad (6.32)$$

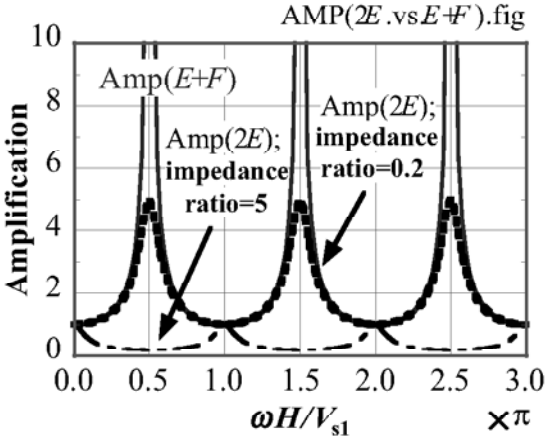

Fig. 6.17 Amplification of two types

Figure 6.17 compares Amp(E + F) and Amp(2E) for the case of impedance ratio $\rho_1 V_{s1}/\rho_2 V_{s2}$ = 0.2 and 5. Note that Amp(*2E*) >1 (large surface motion) occurs only when the surface layer is softer (*impedance ratio < 1*). When the surface is harder, the ground motion is reduced.

When the impedance ratio = 1, Amp(*2E*)=*1.0* for any value of ω and hence $E_1 = E_2$. This is a situation of

rock outcrop in which the surface motion is given by $2E_2$ (Fig. 6.18). It is therefore true that Amp($2E$) is the ratio of motions at the surface of soil and at a rock outcrop (Fig. 6.18). It is important that resonance, i.e. infinite amplification of Amp($E+F$), is possible only when there is a vertical variation (gap) in impedance. Amp($2E$) does not take an infinite value even at the resonance frequency. Hence, an infinite surface response does not occur in reality.

6.9 Significance of Outcrop Motion

The amplification in terms of "*2E*" strictly means the increase in the intensity of the incident wave amplitude

$$\mathrm{Amp}(2E)=\frac{2\times(\text{Amplitude of surface incident moion})}{2\times(\text{Amplitude of incident moion in base rock})}=\frac{2E_1}{2E_R}=\frac{\text{Amplitude of surface moion}}{\text{Amplitude of rock outrock motion}},$$

which is the exact amplification in the surface soil.

In contrast, Amp*(E + F)* simply compares the amplitudes of the surface motion and the motion at the bottom. The bottom motion includes the downward propagation of wave, which is the result of the response of the surface soil, and, therefore, Amp*(E + F)* does not directly mean the amplification made by local soil conditions.

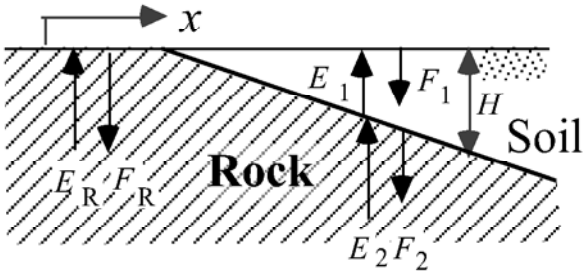

Fig. 6.18 Significance of outcrop motion

When the baserock appears at the surface, it is called a rock outcrop (露頭). Since a rock mass is considered to be uniform and elastic, the nature of the incident motion is identical at both the outcrop and base rock under alluvium, see Fig. 6.18;

$$E_R = E_2,$$

which is assumed to be real and positive without losing generality.

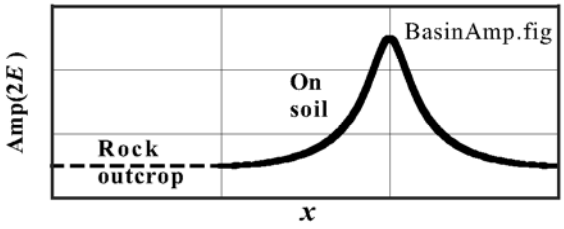

Fig. 6.19 Variation of amplification with local soil conditions

What is recorded upon a rock outcrop is a $2E_R$ motion. Since $E_R = E_2$, the observed rock-outcrop motion can be directly used as an input motion at the bottom of a soil site.

Since the shear stress is zero at the surface of both the outcrop and the soil

$$E_R = F_R \quad \text{and} \quad E_1 = F_1.$$

The surface motion at the outcrop site is given by

$$u_R = 2E_R \exp(i\omega t)$$

Hence, Amp*(2E)* upon rock outcrop is equal t*o 1.0.*

The surface motion at the surface of soft alluvial soil has an amplitude of

$$|2E_1|=\frac{2E_2}{\sqrt{\cos^2\frac{\omega H}{V_{s1}}+\left(\frac{\rho_1 V_{s1}}{\rho_2 V_{s2}}\right)^2\sin^2\frac{\omega H}{V_{s1}}}}=\frac{2E_R}{\sqrt{\cos^2\frac{\omega H}{V_{s1}}+\left(\frac{\rho_1 V_{s1}}{\rho_2 V_{s2}}\right)^2\sin^2\frac{\omega H}{V_{s1}}}},$$

where $\rho_1 V_{s1}/\rho_2 V_{s2}$ is called the impedance ratio. Consequently, Amp*(2E)* at a soil site is given by

$$\mathrm{Amp}(2E)=\frac{1}{\sqrt{\cos^2\frac{\omega H}{V_{s1}}+\left(\frac{\rho_1 V_{s1}}{\rho_2 V_{s2}}\right)^2\sin^2\frac{\omega H}{V_{s1}}}}, \qquad (6.33)$$

as shown by (6.31). Figure 6.19 indicates the variation of Amp($2E$) along the x axis. Since H varies with x, Amp($2E$) changes in the horizontal direction as well. The maximum amplification occurs at some distance from the edge of a soft alluvial plane where the condition of resonance is satisfied. According to (6.33), this maximum amplification is governed by the impedance ratio. Thus, the softer deposit of soil is subjected to the greater amplification and the more seismic risk.

It is not uncommon that a studied ground consists of many different types of soils. The surface fill is underlain by clayey and sandy soils possibly together with gravel. When this is the case, it is a common practice to assume a horizontally layered stratification (Fig. 6.20) in which layers of different soils are stacked in the horizontal direction.

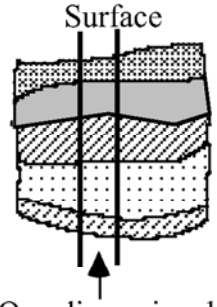

Fig. 6.20 Horizontally layered stratification

In reality, there is a variation of soil type in the horizontal direction. Figure 6.21 compares boring logs from two drilled holes that are only 4 m apart. Although the difference in logs depends on the personal interpretation of the engineer in charge, the two logs do not appear identical. It means that a two-dimensional analysis with this variation taken into account may be required. However, it is practically difficult to run many field investigation (drilling bore holes) and to precisely understand the horizontal variation. Thus, a one-dimensional analysis on a vertical soil column (Fig. 6.22) is commonly practiced today.

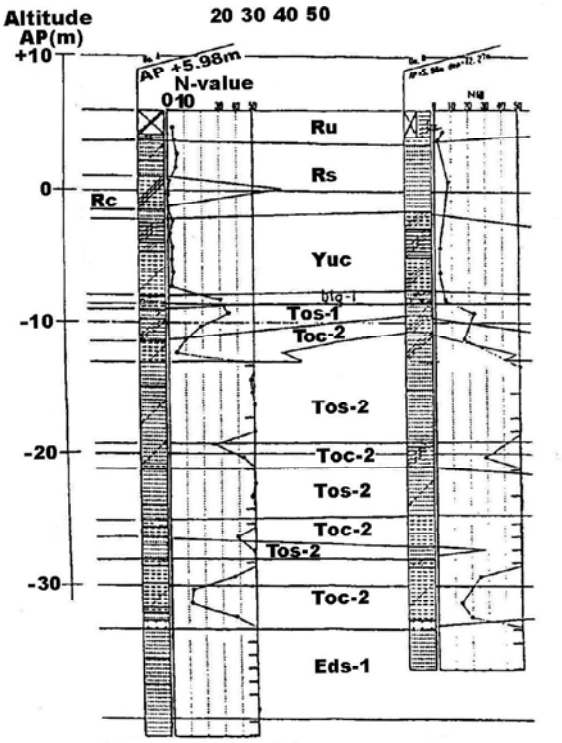

Fig. 6.21 Two boring logs at Shin-Ohta site in Tokyo (by ADEP)

When a harmonic shaking is assumed, each layer has a closed-form solution of displacement and shear stress. In the layer "j" with an elastic property of $G = \rho V_s^2$,

$$u_j = E_j \exp\left\{i\omega\left(t + \frac{z - z_j}{V_{sj}}\right)\right\} + F_j \exp\left\{i\omega\left(t - \frac{z - z_j}{V_{sj}}\right)\right\}$$

$$\tau_j = \mathrm{i}\omega\rho_j V_{sj}\left[E_j \exp\left\{i\omega\left(t + \frac{z - z_j}{V_{sj}}\right)\right\} - F_j \exp\left\{i\omega\left(t - \frac{z - z_j}{V_{sj}}\right)\right\}\right],$$

in which z_j is the depth at the top of this layer (Fig. 6.22). An elastic formula of $G = \rho V_s^2$ was used. Since both displacement "u" and shear stress "τ" are continuous at a layer interface,

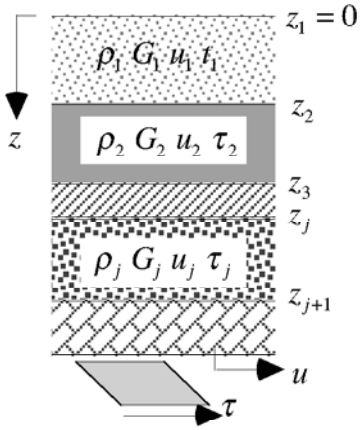

Fig. 6.22 Idealized ground for one-dimensional analysis

$$E_j \exp\left(i\omega\frac{z_{j+1} - z_j}{V_{sj}}\right) + F_j \exp\left(-i\omega\frac{z_{j+1} - z_j}{V_{sj}}\right) = E_{j+1} + F_{j+1}$$

$$\rho_j V_{sj}\left\{E_j \exp\left(i\omega\frac{z_{j+1} - z_j}{V_{sj}}\right) - F_j \exp\left(-i\omega\frac{z_{j+1} - z_j}{V_{sj}}\right)\right\} = \rho_{j+1} V_{sj+1}\left(E_{j+1} - F_{j+1}\right). \quad (6.34)$$

Note that z_{j+1}–z_j stands for the thickness of layer "j". This set of equation makes it possible to describe E_{j+1} and F_{j+1} in terms of E_j and F_j. Moreover, since the shear stress is zero at the ground surface, E_1=F_1. Consequently, all the E_j and F_j, including those in the baserock, are described in terms of E_1. Thus, it becomes possible to calculate the amplification in a multilayered ground.

Many boring logs show a thin soft layer of clay. A one-dimensional analysis that precisely considers this soft layer gives very small surface motion; wave energy is reflected back into the earth by this layer. Is this calculated motion reliable? Yes, it is, if the layer extends to a wide range. In practice, however, a thin layer (<50 cm, e.g.) is eliminated from analysis because it is probably a local clay pocket (deposit).

At the time of 1993 Kushiro-Oki earthquake (釧路沖地震), the maximum acceleration exceeded 900 Gal (=cm/s^2) at the Kushiro Meteorological Observatory (釧路気象台), which was located at the top of a hill (Fig. 6.23). Although this record was surprisingly strong among previous records so-far measured at the ground surface (not inside high buildings), it did not cause structural damage to the observatory building except that shelves and other objects inside fell down to the floor. The reduced damage in the structure was probably because the maximum acceleration continued for a very short time (spiky impact). After this quake, many accelerometers were installed in the Kushiro City and the 1994 Hokkaido-Toho-Oki earthquake (北海道東方沖地震) was recorded. Again the acceleration at the observatory was the greatest (Fig. 6.24), greater than those in the alluvial plane.

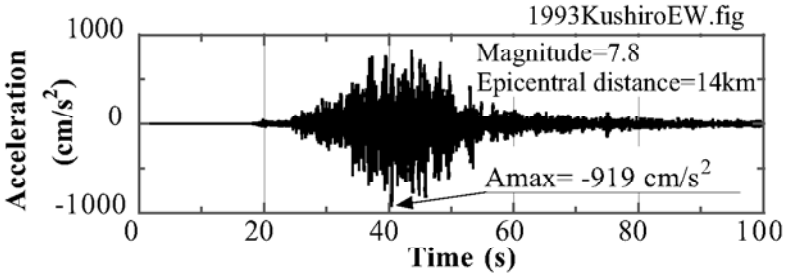

Fig. 6.23 EW acceleration record at Kushiro Meteorological Observatory in 1993 (JSSMFE, 1994)

It is noteworthy that a spiky strong acceleration is not a big problem to structures. This is because it does not give a sufficient time to cause large deformation/displacement (see Sects. 12.1 and 12.2).

Another striking record was the one greater than 1,800 Gal (1.8 times *gravity*) at Tarzana near Los Angeles during the 1994 Northridge earthquake (Fig. 6.25). Although this motion was not spiky, the damage was still relatively light, see Fig. 7.4. During the 1995 Kobe earthquake, the Kobe Meteorological Observatory, which was located at the top of a small hill, recorded 818 Gal in the NS direction that was greater than what were recorded at other stations (Table 7.1). Onishi et al. (1999) collected many records observed at the Kushiro Observatory to show that this site is of greater acceleration than other sites. It is very interesting that both the Kushiro Observatory and the Tarzana sites are located at the top of a small hill (Fig. 6.26). This suggests a topographical amplification of earthquake motion (地形による地震動の増幅).

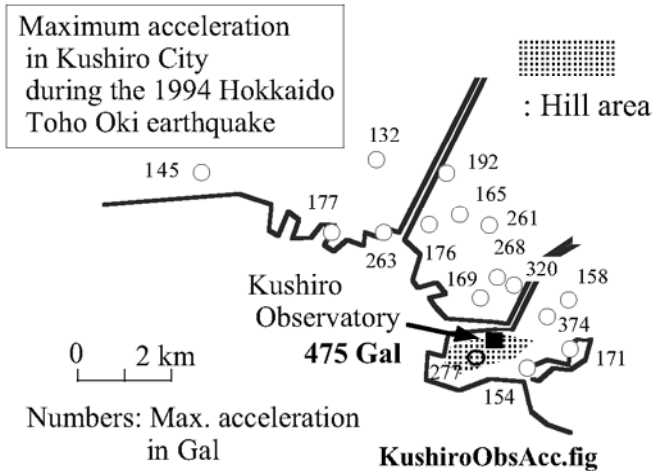

Fig. 6.24 Distribution of the maximum acceleration in Kushiro City recorded in 1994 (WCEE, 1996)

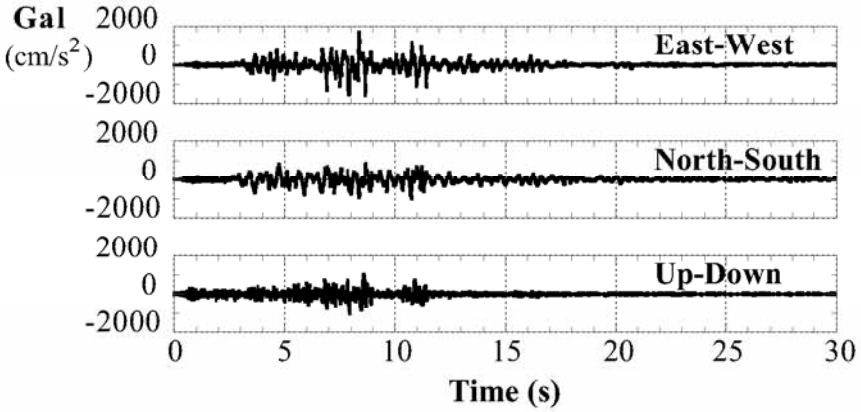

Fig. 6.25 Acceleration at Tarzana during the 1994 Northridge earthquake (epicentral distance = 7km)

Fig. 6.26 Landscape from top of small hill at Tarzana site

It seems that the shape of a hill concentrates the energy of an earthquake motion to its top because the width of a hill decreases at higher elevations. Bear in mind, however, that thus amplified motion does not necessarily induce a heavy damage to structures, although the acceleration is strong. To account for the hill effects, an analysis is made of propagation of SH wave (Sect. 4.2) in a simplified model of two-dimensional topography in Fig. 6.27. Since the attention is focused on the topography, the material properties are uniform.

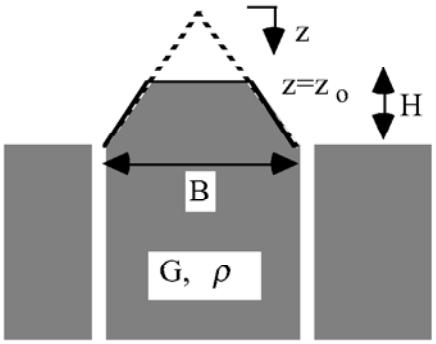

Fig. 6.27 2-D simplified model of hill subjected to horizontal shaking

The model consists of a hill that rests on a vertical column of base rock. G and ρ stand for the elastic shear modulus and the mass density in both hill and base. The geometry of the hill gives the following expressions,

Width of hill = $Bz/(z_0+H)$ and Shear force $=Bz/(z_0+H)\times\tau$ for $z_0 \le z \le z_0+H$ in which τ is the shear stress. When "u" designates the horizontal displacement, the equation of motion of horizontal shaking is derived as

$$\rho B\frac{z}{z_0+H}\frac{\partial^2 u}{\partial t^2}=\frac{\partial}{\partial z}\left(B\frac{z}{z_0+H}\tau\right)=\frac{\partial}{\partial z}\left(B\frac{z}{z_0+H}G\frac{\partial u}{\partial z}\right)\quad\text{and therefore,}\quad z\frac{\partial^2 u}{\partial t^2}=V_s^2\frac{\partial}{\partial z}\left(z\frac{\partial u}{\partial z}\right),$$

where $V_s=\sqrt{G/\rho}$. By assuming a harmonic oscillation, $u(z,t)=U(z)\ \exp(i\omega t)$,

$$V_s^2 z\frac{\mathrm{d}^2U}{\mathrm{d}z^2}+V_s^2\frac{\mathrm{d}U}{\mathrm{d}z}+\omega^2 zU=0\ \text{ and, hence, }\ U=C_1J_0\left(\frac{\omega z}{V_s}\right)+C_2Y_0\left(\frac{\omega z}{V_s}\right),$$

in which J_0 and Y_0 are Bessel functions of the first and second kinds. Theories of Bessel functions are briefly described in Sect. 6.15. Accordingly, the shear stress at the bottom of the hill ($z = H$) is given by

$$\tau=G\left(\frac{\mathrm{d}U}{\mathrm{d}z}\right)\exp(i\omega t)=-\omega\sqrt{\rho G}\left[C_1J_1\left\{\frac{\omega(z_0+H)}{V_s}\right\}+C_2Y_1\left\{\frac{\omega(z_0+H)}{V_s}\right\}\right]\exp(i\omega t)$$

for which a formula of $\mathrm{d}J_0(x)/\mathrm{d}x=-J_1(x)$ was used.

In the elastic base, the conventional solution of S-wave propagation is valid

$$u=E\ \exp\left\{i\omega\left(t+\frac{z-z_0-H}{V_s}\right)\right\}+F\ \exp\left\{i\omega\left(t-\frac{z-z_0-H}{V_s}\right)\right\}$$

At the top of the base, $u=(E+F)\ \exp(i\omega t)$ and $\tau=i\omega\sqrt{\rho G}(E-F)\ \exp(i\omega t)$. By considering the continuity of "u" and "τ" between the hill and the base ($z = z_0+H$) together with the boundary condition of $\tau=0$ at the top of the hill ($z = z_0$),

$$\begin{Bmatrix}C_1\\C_2\end{Bmatrix}=\frac{2iE\begin{Bmatrix}Y_1(\omega z_0/V_s)\\-J_1(\omega z_0/V_s)\end{Bmatrix}}{\left[J_0\left\{\frac{\omega(z_0+H)}{V_s}\right\}Y_1\left(\frac{\omega z_0}{V_s}\right)-J_1\left(\frac{\omega z_0}{V_s}\right)Y_0\left\{\frac{\omega(z_0+H)}{V_s}\right\}\right]}$$

$$-i\left[J_1\left\{\frac{\omega(z_0+H)}{V_s}\right\}Y_1\left(\frac{\omega z_0}{V_s}\right)-J_1\left(\frac{\omega z_0}{V_s}\right)Y_1\left\{\frac{\omega(z_0+H)}{V_s}\right\}\right]$$

$$F=-E+C_1J_0\left\{\frac{\omega(z_0+H)}{V_s}\right\}+C_2Y_0\left\{\frac{\omega(z_0+H)}{V_s}\right\}.$$

Consequently, amplifications produced by a hill topography are derived as

$$\mathrm{Amp}(2E)=\left|\frac{U(z_0)}{2E}\right| = \frac{2V_s/\pi\omega z_0}{\sqrt{\left[J_0\left\{\frac{\omega(z_0+H)}{V_s}\right\}Y_1\left(\frac{\omega z_0}{V_s}\right)-J_1\left(\frac{\omega z_0}{V_s}\right)Y_0\left\{\frac{\omega(z_0+H)}{V_s}\right\}\right]^2+\left[J_1\left\{\frac{\omega(z_0+H)}{V_s}\right\}Y_1\left(\frac{\omega z_0}{V_s}\right)-J_1\left(\frac{\omega z_0}{V_s}\right)Y_1\left\{\frac{\omega(z_0+H)}{V_s}\right\}\right]^2}}$$

$$\mathrm{Amp}(E+F)=\left|\frac{U(z_0)}{U(z_0+H)}\right|=\frac{2V_s/\pi\omega z_0}{\left|J_0\left\{\frac{\omega(z_0+H)}{V_s}\right\}Y_1\left(\frac{\omega z_0}{V_s}\right)-J_1\left(\frac{\omega z_0}{V_s}\right)Y_0\left\{\frac{\omega(z_0+H)}{V_s}\right\}\right|}$$

for which the *Lommel*'s formula, $Y_\upsilon(x)J_{\upsilon+1}(x)-J_\upsilon(x)Y_{\upsilon+1}(x)=2/\pi x$, was employed.

The amplification effects of a hill, Amp(2*E*) and Amp(*E*+*F*), are calculated by using the theory as developed in Sect. 6.12. In this section, five types of the hill shape are employed as illustrated in Fig. 6.28. Among them, Amp(2*E*)=1 and Amp(*E*+*F*)=$\left|1/\cos(\omega H/V_s)\right|$ are known for the case of "Top width = Base width, *B*" at the far right.

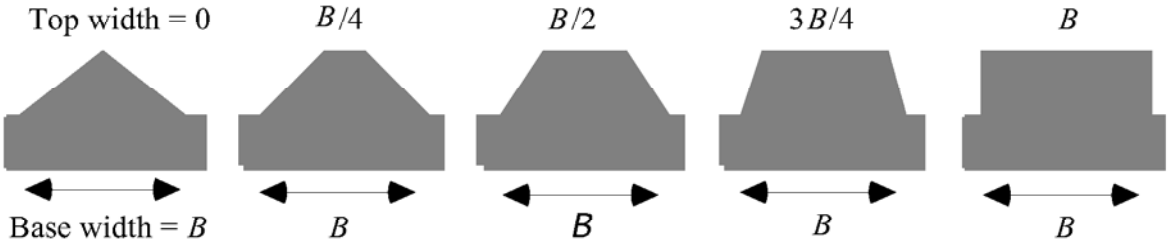

Fig. 6.28 Shapes of the analyzed hill

The calculated amplification, Amp(2*E*), is illustrated in Fig. 6.29. When the top width is shorter than the bottom width, the amplification is always greater than unity irrespective of the shaking frequency. This amplification is equal to the amplitude ratio between the hill top and the surface of low land (Fig. 6.29). It is evident that the triangular hill with the top width = 0 achieves the greatest amplification at all the frequencies. In contrast, the top width = *B* is of Amp(2*E*)=1 at any frequency as the theory of uniform elastic medium states. It seems that the assumption of uniform elasticity is not too bad because real hills are made of relatively harder materials than soft alluvium.

The calculated large amplification for the case of *top width = 0* is reasonable. The seismic energy that is incident at the base travels upwards. As the width of the hill decreases at higher elevations, the energy is concentrated within a limited hill width. Since the greater energy density makes the larger magnitude of shaking (see Sect. 4.11), the case of the zero width at the top demonstrates the largest amplification. Note that Amp(2*E*) in Fig. 6.29 approaches the theoretical value of $\sqrt{\text{width ratio}}$ at higher frequencies. When the top width = *B*/4 for example, the width ratio = 1:4 and the shaking energy density = 4:1. Hence, the amplitude ratio is 2:1.

Figure 6.30 shows Amp(*E*+*F*) of a hill topography. It is interesting that the resonance in a triangular hill (top width = 0) occurs at a frequency higher than those of more trapezoidal or rectangular topographies.

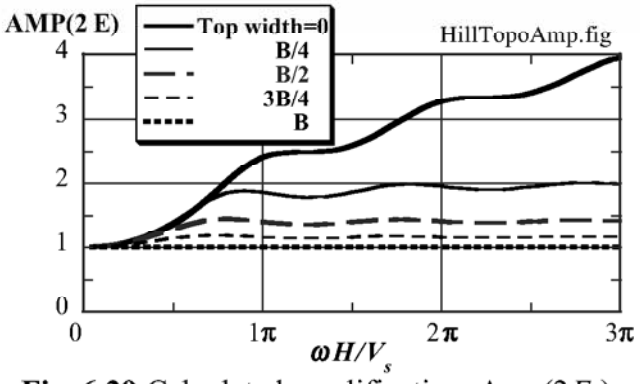

Fig. 6.29 Calculated amplification, Amp(2*E*) at the top of a hill

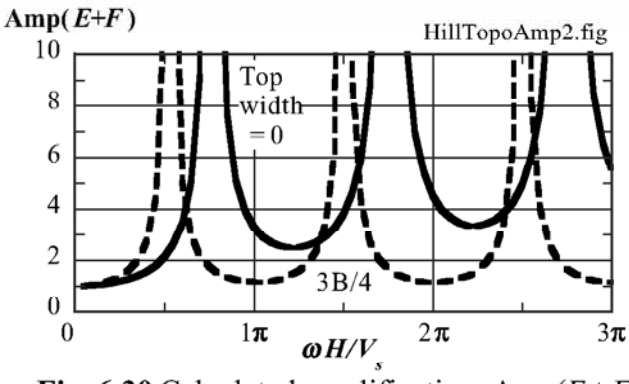

Fig. 6.30 Calculated amplification, Amp(*E*+*F*), at the top of a hill

Further note that the resonance in Amp(*E*+*F*) in Fig. 6.30 does not affect Amp(2*E*) in Fig. 6.29.

Because of numerical reasons in a computer, the width of the top = 0.000999, 0.24999998, 0.500000, 0.750000, and 0.999001 times *B* were employed in the analysis.

After the experience of strong acceleration in Kushiro (Fig. 6.23), earthquake motion has been observed at the site in Kushiro at the surface and bottom of the hill (vertical array observation). In addition to Ohta (1995) who showed amplification between the surface and the foot of the hill slope [Amp(2*E*)], Kanda and Motosaka (1995) as well as Ishida et al. (1996) showed increased acceleration at the surface as compared with that in the bottom layer of the hill. It seems that the amplification between the surface and the bottom includes not only the topographic amplification but also the one due to surface softer material that occurs even in a level topography.

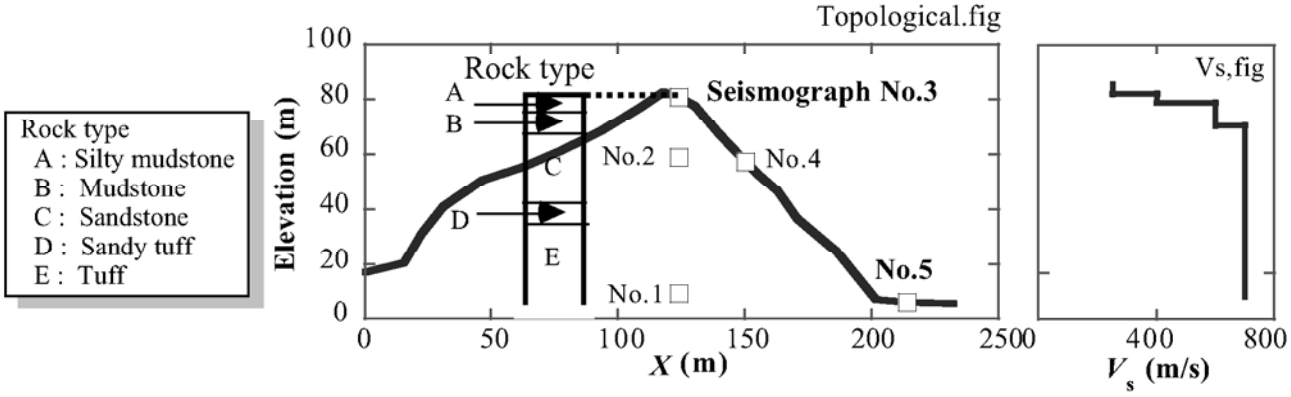

Fig. 6.31 Site of observation of topographic effects on earthquake amplification (after Kurita et al. 2005)

The topographic amplification as calculated in Sect. 6.15 is validated more clearly by another set of observed acceleration time histories during the 1985 Chiba-Toho-Oki earthquake. Kurita et al. (2005) recorded acceleration histories in and on a small hill as shown in Fig. 6.31. The Fourier spectra of acceleration records at two stations, No. 3 at the top and No. 5 at the foot, were calculated and their ratio was obtained as shown in Fig. 6.32. It is seen therein that the spectrum ratio that stands for the amplification of Amp(2*E*) increases with the shaking frequency. This finding is consistent with the findings in Fig. 6.29. The total collapse of houses on a terrace hill in Balakot of Pakistan during the 2005 North Pakistan earthquake (Fig. 6.33) may be the results of this topographic amplification.

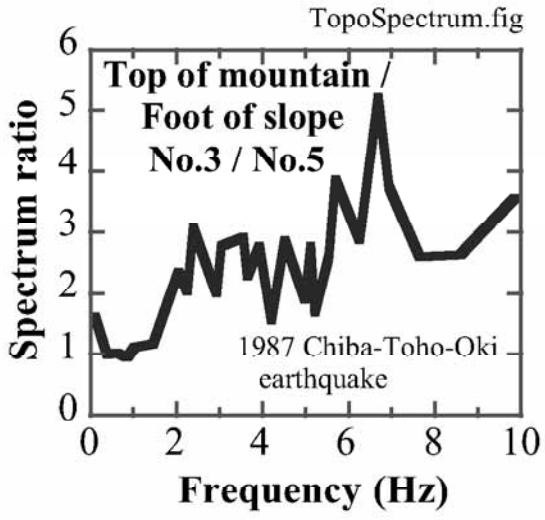

Fig. 6.32 Observed topographic effects on seismic amplification (after Kurita et al., 2005)

Fig. 6.33 Completely destroyed houses on terrace hill in Balakot of Pakistan during 2005 earthquake

Suppose a topography in Fig. 6.34 where the crest angle is given by $\nu\pi$. Midorikawa (1999) presented an empirical knowledge that the hill-top motion is amplified by $1/\nu$, irrespective of shaking frequency, as compared with the motion on a free field. Kurita et al. (2005) presented the maximum horizontal accelerations that were observed at the top and the foot of a mountain. With reference to the topography

of the mountain in Fig. 6.31, the value of ν is 0.57. This value suggests the amplification of 1.75. The real amplification in Fig. 6.35, however, is greater than $1/\nu$.

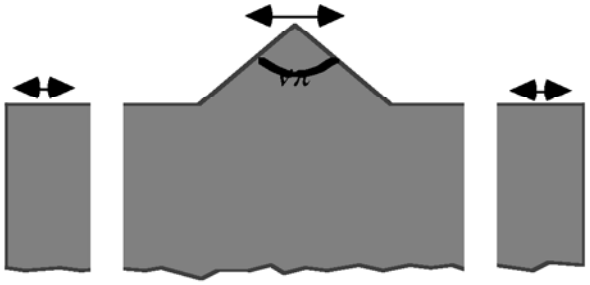

Fig. 6.34 Schematic topography of hill

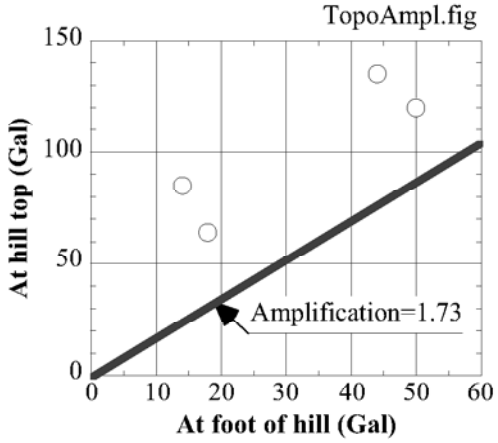

Fig. 6.35 Comparison of observed and assessed amplification of maximum acceleration

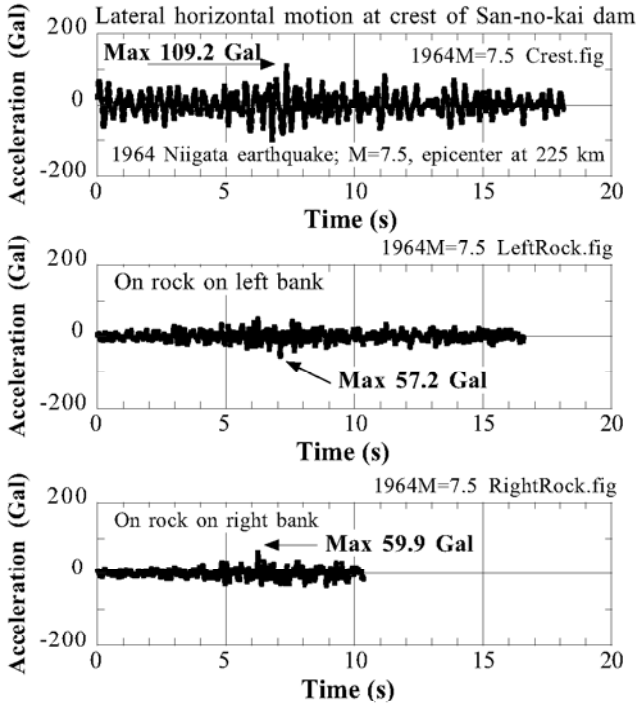

Fig. 6.36 Response of San-no-kai dam during the 1964 Niigata earthquake (data by Tamura, 1996)

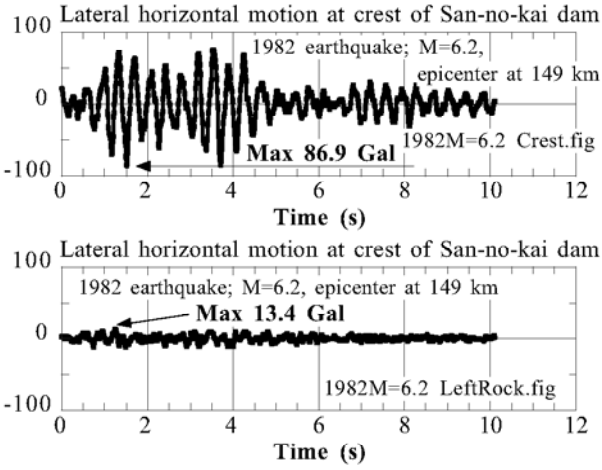

Fig. 6.37 Response of San-no-kai dam during a minor seismic event (data by Tamura, 1996)

It is interesting to discuss seismic response and amplification in a dam. San-no-kai Dam (山王海ダム) is an earth-fill dam which measures 37 m in height and 145 m in length. Its earthquake response has been monitored since 1960s (Tamura, 1996) and records of two quakes are compared in what follows.

Figure 6.36 compares the acceleration records during the 1964 Niigata earthquake (Magnitude = 7.3). In the top of this figure, the motion in the transverse direction (in the direction of valley) at the crest (top) of the dam is indicated. The maximum acceleration is 109 Gal. In the rock abutment on the left bank, the motion was smaller (57.2 and 59.9 Gal). By considering this rock motion as the outcrop motion, the amplification of Amp(2*E*) is derived as 109.2/57.2 = 1.91 and 109.2/59.9 = 1.82. In contrast, Figure 6.37 presents the record during a minor earthquake in 1982 (Magnitude = 6.2). The maximum accelerations at the crest and at the left abutment are 86.9 Gal and 13.4 Gal, respectively, making Amp(2*E*) = 6.49. Thus, the amplification during these two earthquakes are completely different due probably to nonlinear stress–strain nature of soil (Chap. 9). More in detail, the stronger earthquake developed larger shear strain in soil and made the shear modulus smaller, while damping ratio was made greater. Hence, the amplification was reduced. The amplification thus depends on the shear strain during shaking.

6.15 Theory of Bessel Functions

The theory of Bessel functions (e.g., Wylie, 1975) states that a Bessel´s differential equation of order υ;

$$x^2\frac{\mathrm{d}^2y}{\mathrm{d}x^2}+x\frac{\mathrm{d}y}{\mathrm{d}x}+\left(x^2-\upsilon^2\right)y=0 \tag{6.35}$$

has a solution of

$$y=C_1J_\upsilon(x)+C_2Y_\upsilon(x),$$

where J and Y are Bessel´s functions of the first and the second types, respectively, while two constants of C_1 and C_2 are determined so that boundary or initial conditions may be satisfied. Thus, Bessel functions of J and Y in (6.35) play such roles that are similar to those of sin and cos functions in a harmonic differential equation.

When x is sufficiently large, the following approximate relationships hold true

$$J_\upsilon(x)\approx\sqrt{\frac{2}{\pi x}}\cos\left(x-\frac{\pi}{4}-\frac{\upsilon\pi}{2}\right)\quad\text{and}\quad Y_\upsilon(x)\approx\sqrt{\frac{2}{\pi x}}\sin\left(x-\frac{\pi}{4}-\frac{\upsilon\pi}{2}\right).$$

When x is very small, conversely, and υ is not zero, the series solution of (6.35) suggests

$$J_\upsilon(x)\approx\frac{1}{\Gamma(1+\upsilon)}\left(\frac{x}{2}\right)^\upsilon\quad\text{and}\quad Y_\upsilon(x)\approx\frac{-1}{\sin\upsilon\pi\Gamma(1-\upsilon)}\left(\frac{2}{x}\right)^\upsilon,$$

where Γ stands for a Gamma function and $\Gamma(n)=(n-1)!=(n-1)(n-2)(n-3)\cdots2\cdot1$ when n = 1, 2, 3, 4, $\cdots$.

Bessel functions give a set of general solutions for a differential equation that takes the form of

$$x^2\frac{\mathrm{d}^2y}{dx^2}+x\left(a+2bx^p\right)\frac{dy}{dx}+\left\{c+dx^{2q}+b(a+p-1)x^p+b^2x^{2p}\right\}y=0.$$

The solution is given by

$$y=x^\alpha\ \exp\left(-\beta x^p\right)\left\{C_1J_\upsilon\left(\lambda x^q\right)+C_2Y_\upsilon\left(\lambda x^q\right)\right\},$$

in which

$$\alpha=(1-a)/2,\quad\beta=b/p,\quad\lambda=\sqrt{|d|}/q,\quad\text{and}\quad\upsilon=\sqrt{(1-a)^2-4c}\,/(2q),$$

Differentiation of Bessel functions is made possible by

$$\frac{\mathrm{d}J_\upsilon(x)}{\mathrm{d}x}=\frac{\upsilon}{x}J_\upsilon(x)-J_{\upsilon+1}(x)\quad\text{and}\quad\frac{\mathrm{d}Y_\upsilon(x)}{\mathrm{d}x}=\frac{\upsilon}{x}Y_\upsilon(x)-Y_{\upsilon+1}(x).$$

Finally, the Lommel´s formula is important

$$Y_\upsilon(x)J_{\upsilon+1}(x)-J_\upsilon(x)Y_{\upsilon+1}(x)=\frac{2}{\pi x}.$$

Numerical analysis on seismic response of two-dimensional or three-dimensional shape (embankment, foundation of structure, etc.) is often conducted by finite element or finite difference formulations. It is commonly the case that those numerical methods work on a limited part of ground although the real ground has an infinite size (Fig. 6.38). This discrepancy may cause such a problem that the downward propagation of seismic motion is reflected at an artificial boundary of the domain of analysis while in reality the motion goes back into the infinite half space (see one-dimensional example in Fig. 6.39).

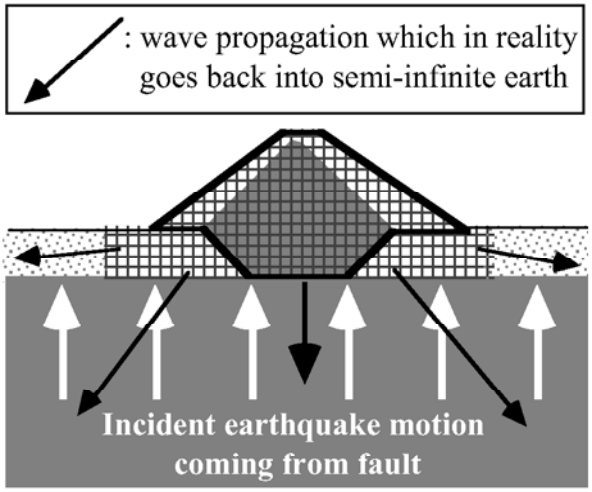

Fig. 6.38 Numerical analysis on limited size of model out of infinite halfspace

To remove the seismic wave energy that is reflected at the artificial boundary, a special boundary condition is needed, which accounts for an infinite size of the real ground. Without making reflection of wave, this kind of boundary condition is called energy absorbing boundary, energy transmitting boundary, silent boundary, transparent boundary, infinite boundary, etc.

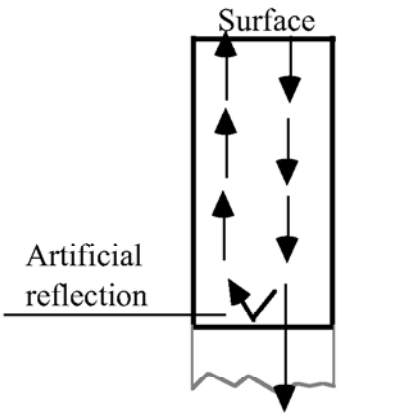

Fig. 6.39 Artificial reflection of seismic energy at boundary of numerical model

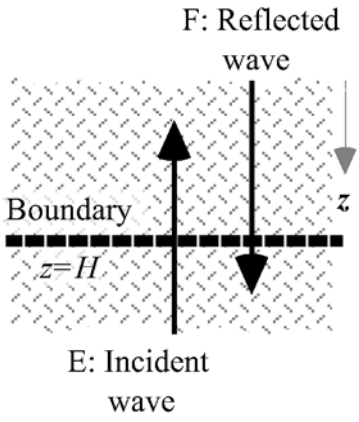

Fig. 6.40 Vertical wave propagation at engineering base rock of one-dimensional model

The simplest energy absorbing boundary was proposed by Joyner (1975). Fig. 6.40 illustrates that a boundary is placed in an engineering base rock, which is actually not necessarily a real rock layer but possibly pleistocene or tertiary hard soil (V_s=500 m/s for example). It is a convention to treat this base as an elastic medium. In a one-dimensional vertical wave propagation, the S-wave propagation at the base is expressed by an elastic model

$$u = E\left(t + \frac{z}{V_s}\right) + F\left(t - \frac{z}{V_s}\right), \qquad (6.36)$$

in which E and F are arbitrary functions, u stands for lateral displacement and V_s is the S-wave velocity in the base rock. Note that S wave consists of superposition of incident and reflected waves (Sect. 4.4), and it is aimed by an infinite boundary to erase the F component (Fig. 6.40). Accordingly, velocity, v, and shear stress produced by S-wave motion are given by

$$v = \frac{\partial u}{\partial t} = E'\left(t + \frac{z}{V_s}\right) + F'\left(t - \frac{z}{V_s}\right) \quad \text{and}$$

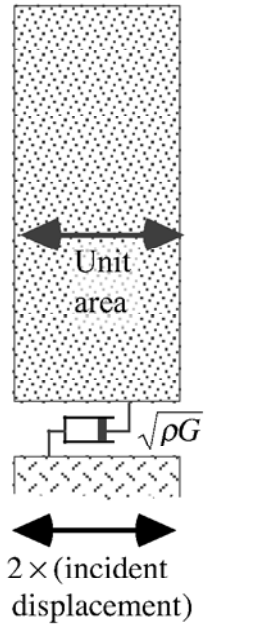

Fig. 6.41 Mechanism of viscous boudary condition

$$\tau = G\frac{\partial u}{\partial z} = \sqrt{\rho G}\left[E'\left(t+\frac{z}{V_s}\right) - F'\left(t-\frac{z}{V_s}\right)\right], \qquad (6.37)$$

where E' stands for a derivative of E. Note that the first term of the velocity formula gives the velocity induced by the incident wave, v_I, which is produced by fault mechanism and wave propagation in the elastic earth

$$v_I = E'\left(t+\frac{z}{V_s}\right). \qquad (6.38)$$

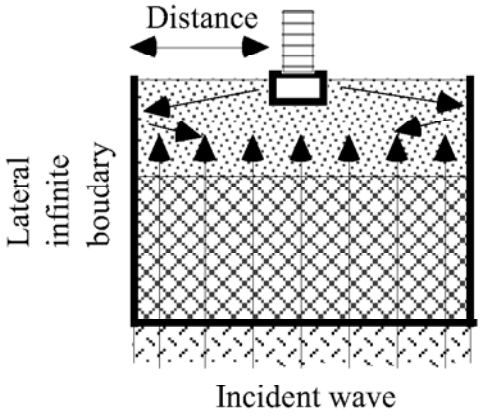

Fig. 6.42 Two-dimensional idea of viscous boudary condition

It is then interesting that shear stress and velocity are related with each other by

$$\tau = \sqrt{\rho G}\left(2v_I - v\right). \qquad (6.39)$$

This implies that the soil mass above the boundary is shaken by shear stress (6.39) in the base which is equal to a velocity difference, $2v_I - v$, multiplied by $\sqrt{\rho G}$. This idea as proposed by Joyner (1975) is illustrated in Fig. 6.41 to show that the effects of elastic infinite medium is numerically reproduced by connecting the surface soil layer with $2\times$(the incident soil motion) by means of a dashpot of $\sqrt{\rho G}$. Thus, the energy of incident wave is transmitted through the dashpot into the surface soil, while the energy of the reflected wave is absorbed.

The viscous boundary condition in Fig. 6.41 is able to absorb the reflected S wave perfectly in a one-dimensional case. For P wave, furthermore, a similar dashpot is installed in the vertical direction, for which G is replaced by (Young´s modulus)$\times(1-\nu)$ /$\{(1+\nu)(1-2\nu)\}$; lateral distortion being confined (K_o condition) as is the case in an infinite level ground.

The viscous boundary perfectly absorbs wave energy when P and S waves propagate perpendicular to the boundary. When the wave propagation direction is oblique, which is often the case in a two (or three)-dimensional analysis (Fig. 6.42), the efficiency decreases (Lysmer and Kuhlemeyer, 1969; Lysmer and Waas, 1972). In this regard, White et al. (1977) attempted to optimize the dashpot coefficients for the minimal reflection of wave energy.

There are many more techniques of infinite boundary. Clayton and Engquist (1977) used what is called a paraxial equation in place of the conventional wave propagation equation. When displacement is designated by u, a paraxial equation of S wave propagation is written as

$$\frac{\partial^2 u}{\partial t^2} = V_s\frac{\partial^2 u}{\partial x \partial t}. \qquad (6.40)$$

The solution of this paraxial equation is evidently given by

$$u = E\left(t+\frac{x}{V_s}\right), \qquad (6.41)$$

which implies that wave propagates only in the negative direction of x coordinate.

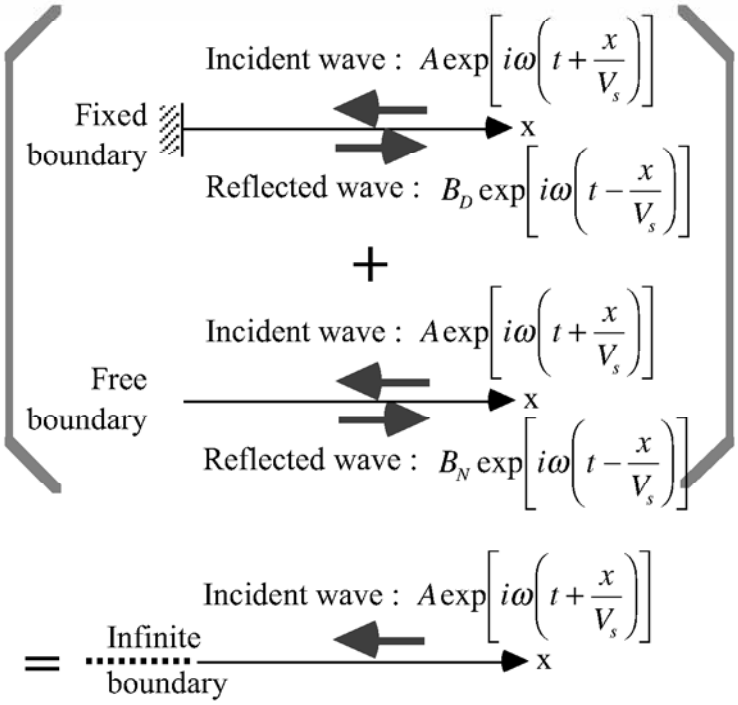

Fig. 6.43 Superposition of fixed (Dirichlet) and free (Neumann) boundary conditions for infinite boundary condition

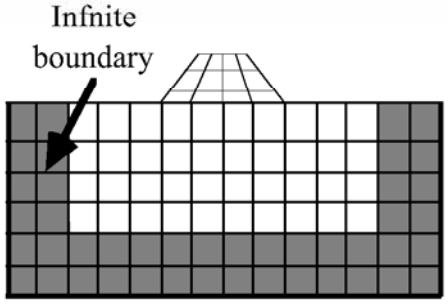

Fig. 6.44 Infinite boundary zone for superposition boundary in two-dimensional analysis

In contrast to the conventional wave propagation equation (solution is (6.36)), which allows wave propagation in both positive and negative directions of spatial coordinate, the paraxial equation allows wave propagation only in one direction. Thus, waves can propagate only in the outward direction at the infinite boundary, and no reflection is possible. This idea was used by Akiyoshi et al. (1994) as well. Cohen and Jennings (1983) demonstrated its application to a simple one-dimensional wave propagation. Note that both viscous and paraxial boundaries assume the infinite space to be linearly elastic.

Smith (1974) developed a different infinite boundary technique in which solutions from two different but conventional boundary conditions are superimposed. When the wave that arrives at the boundary is specified by a harmonic function, for example, of $A\ \exp\left[i\omega\left(t+x/V_s\right)\right]$ (Fig. 6.43), the fixed boundary (zero displacement at $x = 0$) gives a reflected wave such as

$$\text{Reflected wave at fixed boundary} = B_D\ \exp\left[i\omega\left(t-\frac{x}{V_s}\right)\right] = -A\ \exp\left[i\omega\left(t-\frac{x}{V_s}\right)\right]. \qquad (6.42)$$

In contrast when the boundary is free (zero shear stress),

$$\text{Reflected wave at free boundary} = = B_N\ \exp\left[i\omega\left(t-\frac{x}{V_s}\right)\right] = A\ \exp\left[i\omega\left(t-\frac{x}{V_s}\right)\right]. \qquad (6.43)$$

By superposing (6.42) and (6.43) and then dividing by 2, the reflected wave is made null, while maintaining the incident wave unchanged. In practice of analysis, calculation is conducted twice with different boundary conditions and the solutions are added and divided by two. This superposition boundary has been used by Cundall et al. (1978), Kausel and Tassoulas (1981), Kunar and Rodriquez-Ovejero (1980), and Kunar (1982). This boundary condition works in a time-domain analysis in which an equation of motion is integrated along the time axis.

In practice of two-dimensional analysis, the reflected wave may hit another boundary and is reflected again. This multiple reflection makes superposition very complicated. To avoid this, the superposition is

conducted periodically after a short specified time interval. Figure 6.44 illustrates an infinite boundary zone and the superposition is conducted before the reflected wave comes out of this zone.

In contrast to the foregoing boundaries that work in time-domain analyses, the energy transmitting boundary by Lysmer and Drake (1971, 1972) as well as Lysmer and Waas (1972) works in frequency-domain analyses, which assume seismic shaking as being superimposed harmonic motions. By considering the ground response to be Rayleigh and Love waves, harmonic stress response near the lateral boundary (Fig. 6.45) is calculated and employed as a lateral boundary condition, thus eliminating artificial wave reflection. This method has been used in combination with viscous boundary at the bottom (Fig. 6.45).

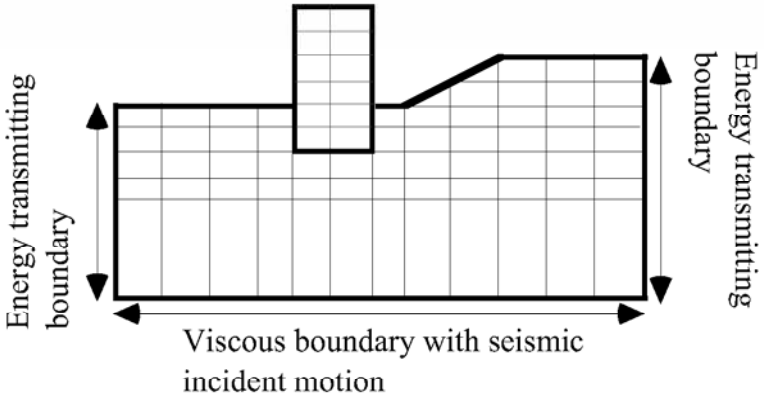

Fig. 6.45 Combination of energy transmitting and viscous boundaries for analyses in frequency domain

The infinite boundaries so far described consist of special mathematical considerations. In spite of this, they have a limitation that nonlinear stress–strain behavior cannot be easily handled. This shortcoming may be significant in analyses of soft ground undergoing strong motion and liquefaction in which soil nonlinearity becomes substantial. Under such situations, elementary and primitive methods may be useful. The simplest method is to locate boundaries at a far distance from the area of interest; making "distance" in Fig. 6.42 large enough. This implies that energy dissipation due to nonlinearity (stress–strain loop) makes waves decay during propagation and the unfavorably reflected wave does not affect the calculated response in the interested zone. The lateral boundary may be (1) free horizontal motion and zero vertical motion (Fig. 6.46), or (2) repeated boundary (Fig. 6.47) for a symmetric geometry. Note that static active failure of a vertical lateral boundary has to be prevented by, for example, applying Ko static earth pressure in Fig. 6.46. Fixing the vertical displacement prevents ground subsidence during shaking and may not be appropriate. On the other hand, the repeated boundary makes horizontal motions at both right and left sides equal to each other and implies that identical model is repeated in the horizontal direction. This situation is similar to that in a laminar box (Sect. 24.13) in shaking model tests. Note again that lateral boundaries should be located at a sufficiently far distance so that the reflected wave may be too weak to affect the calculated response in the central part.

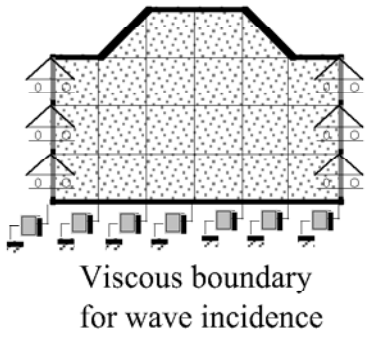

Fig. 6.46 Horizontally free boundary.

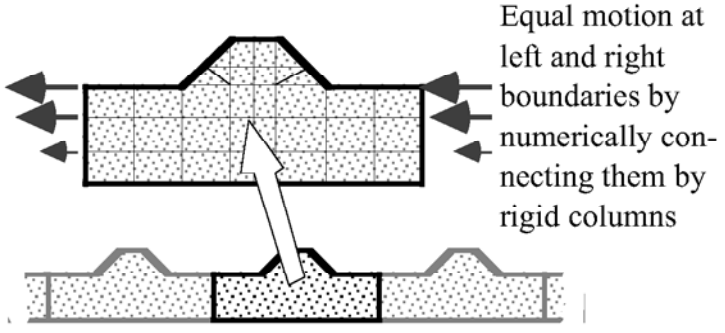

Fig. 6.47 Repeated lateral boundary

There are more attempts so far made to produce infinite boundary conditions. For example, Akao and Hakuno (1983) predicted the displacement at an infinite boundary by using previous boundary displacement together with displacement inside the domain of analysis. In 1980s the author and Dr. O.Al-Hunaidi tried to develop an energy absorbing boundary for 2- or 3-dimensional nonlinear analysis in the time domain. The idea was to remove numerically the kinematic energy near the boundary while fixing the strain energy therein. This was however difficult and the attempt was incomplete.

6.17 Exercise No. 2 of Dynamic Response Analysis on Elastic Ground

Figure 6.48 illustrates a topography of a horizontal free field and rock outcrop. Material properties and elastic and parameters are supplied in the figure.

1. Assume harmonic motion ($\sin\omega t$ and $\cos\omega t$) and express the amplitudes of F_1, E_2, F_2, E_1', and F_1' as functions of E_1.
2. Plot Amp(E+F) and Amp($2E$) against $\omega H/V_{s1}$ in which ω is the circular frequency of motion. You can assume two kinds of the impedance ratio $\left(\rho_1 V_{s1}/\rho_2 V_{s2}\right)$.
3. Suppose that the earthquake displacement at the surface of outcrop is expressed by

$$u_{\text{outctop}}(t) = 0.02\ \sin 2\pi t + 0.01\ \cos 6\pi t + 0.002\ \sin 20\pi t \qquad (6.44)$$

as plotted in Fig. 6.49. Calculate and plot the function of the acceleration time history at the top of the outcrop.

4. Suppose H=12 m, V_{s1}=150 m/s, and V_{s2}=800 m/s. Assume any realistic values for mass density of soils. Calculate and plot the time history of displacement at the surface of the alluvial deposit.
5. Calculate and plot the acceleration time history at the surface of the alluvial deposit.
6. Compare maximum values of displacement and acceleration at the surface of alluvium and the outcrop.

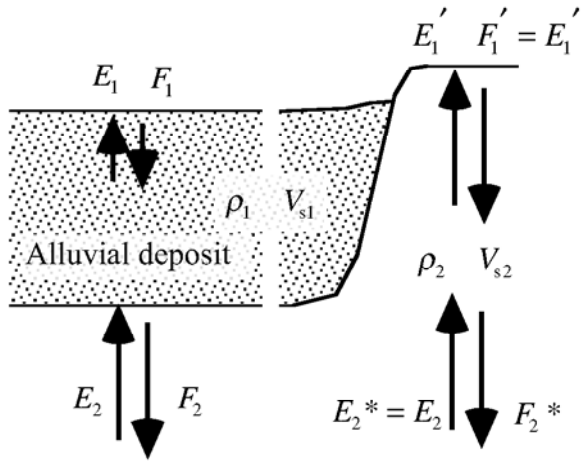

Fig. 6.48 Model of free field and rock outcrop

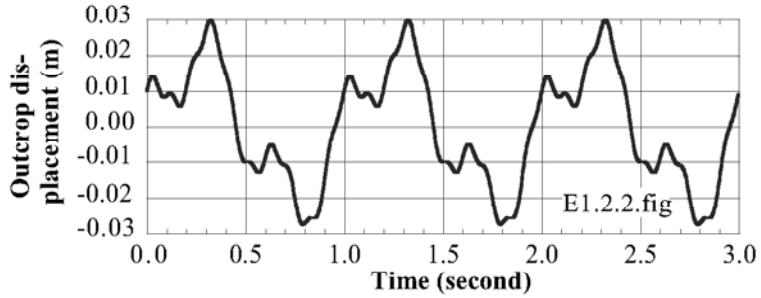

Fig. 6.49 Displacement time history at outcrop

List of References in Chapter 6

Akao, Y. and Hakuno, M. (1983) Dynamic analysis of wave propagation procedure on the infinite boundary, Proc. JSCE, No, 336, pp. 21–29 (in Japanese).

Akiyoshi, T., Fuchida, K. and Fang, H.L. (1994) Absorbing boundary condition for dynamic analysis of fluid-saturated porous media, Soil Dynam. Earthq. Eng., Vol. 13, pp. 387–397.

Clayton, R. and Engquist, B. (1977) Absorbing boundary conditions for acoustic and elastic wave equations, Bull. Seism. Soc. Am., Vol. 67, No. 6, pp. 1529–1540.

Cohen, M. and Jennings, P.C. (1983) Silent boundary methods for transient analysis, Computational Methods for Transient Analysis, Vol. 2, Computational Methods in Mechanics, Elsevier, New York, Chap. 7, pp. 301–360.

Cundall, P.A., Kunar, R.R., Carpenter, P.C. and Marti, J. (1978) Solution of infinite dynamic problems by finite modelling in the time domain, Proc. 2nd Int. Conf. Appl. Num. Modelling, pp. 339–351.

Hardin, B.O. and Drnevich, V.P. (1972) Shear modulus and damping in soils : measurement and parameter effects, Proc. ASCE, Vol. 98, SM6, pp. 603–624.

Ishida, H., Sasaki, T., Niwa, M., Kitagawa, Y. and Kashima, T. (1996) Amplification characteristics of surface layers obtained from earthquake observation records of vertical instrument arrays at Kushiro local meteorological observatory, J. Struct. Construct. Eng., Architectural Inst. Japan, Vol. 490, pp. 91–100 (in Japanese).

Japan Electricity Association 日本電気協会 (1998) Guideline for earthquake resistant design of electric facilities in transformer substations etc., 変電所等における電気設備の耐震設計指針, JEAG 5003-1998.

Joyner, W.B. (1975) Method for calculating nonlinear seismic response in two dimensions, Bull. Seismol. Soc. Am., Vol. 65, No. 5, pp. 1337–1357.

JSSMFE (1994) Damage investigation report of the 1993 Kushiro-oki and Noto-Hanto-oki earthquakes, p. 25 (in Japanese).

Kanda, K. and Motosaka, M. (1995) The evaluation of effects of spatial variability of soil properties, surface topography and spatial coherency of incident wave on ground motion amplification – The case of Kushiro J.M.A. site, J. Struct. Construct. Eng., Architectural Inst. Japan, Vol. 476, pp. 85–94 (in Japanese).

Kausel, E. and Tassoulas, J.L. (1981) Transmitting boundaries; a closed-form comparison, Bull. Seismol. Soc. Am., Vol. 71, No. 1, pp. 143–159.

Kunar, R.R. (1982) A mixed implicit/explicit procedure for soil-structure interaction, Nucl. Eng. Des., Vol. 69, No. 1, pp. 87–93.

Kunar, R.R. and Rodriquez-Ovejero, L. (1980) A model with non-reflecting boundaries for use in explicit soil-structure interaction analyses, Earthq. Eng. Struct. Dynam., Vol. 8, pp. 361–374.

Kurita, T., Annaka, T., Takahashi, S., Shimada, M. and Suehiro, T. (2005) Effects of irregular topography on strong ground motion amplification, Proc. Japan Assoc. Earthq. Eng., Vol. 5, No. 3 (electronic journal in Japanese).

Lefebvre, G. and LeBoeuf, D. (1987) Rate effects and cyclic loading of sensitive clays, J. Geotech. Eng., ASCE, Vol. 113, No. 5, pp. 476–489.

Lysmer, J. and Drake, L.A. (1971) The propagation of Love waves across nonhorizontally layered structures, Bull Seismol. Soc. Am., Vol. 61, No. 5, pp. 1233–1251.

Lysmer, J. and Drake, L.A. (1972) A finite element method for seismology, Methods Comput. Phys., Vol. 11, Academic Press, New York, pp. 181–216.

Lysmer, J. and Kuhlemeyer, R.L. (1969) Finite dynamic model for infinite media, Proc. ASCE, Vol. 95, EM4, pp. 859–877.

Lysmer, J. and Waas, G. (1972) Shear waves in plane infinite structures, Proc. ASCE, Vol. 98, EM1, pp. 85–105.

Midorikawa, S. (1999) Nature of seismic ground motion, Earthquake Motion, Geotech-Notebook No. 9, Japan. Geotech. Soc., pp. 37–64 (in Japanese).

Ohta, T. (1995) Strong ground motions at Kushiro observatory and vibration characteristics of ground and structures, J. Struct Construct. Eng., Architectural Inst. Japan, Vol. 474, pp. 77–85 (in Japanese).

Onishi, J., Yamazaki, F. and Wakamatsu, K. (1999) Relationship between geomorphological land classification and amplification ratio based on JMA strong motion records, Proc. JSCE, 626/I-48, pp. 79–91 (in Japanese).

Proc. Special Theme Session on 'Test-Sites' (STS-16) (1996) 11th World Conf. Earthq. Eng., Acapulco, p. 30.

Smith, W.D. (1974) A nonreflecting plane boundary for wave propagation problems, J. Comput. Phys., Vol. 15, pp. 492–503.

Tamura, C. (1996) Seismic damage and geosphere, publ. Sankai-Do, attached floppy disk (in Japanese).

Togawa, H. (1975) Vibration analysis by FEM, Science Publication, pp. 46–47 (in Japanese).

WCEE (1996) Special Theme Session on TEST-SITES of 11th world Conf. Earthq. Eng., Acapulco, pp.30.

White, W., Valliappan, S. and Lee, I.K. (1977) Unified boundary for finite dynamic models, Proc. ASCE, Vol. 103, EM5, pp. 949–964.

Wylie, C.R. (1975) Advanced Engineering Mathematics, International Student Editions, McGraw-Hill, New York, ISBN 0-07-072180-7, pp.388-440.

Chapter 7

Pseudostatic

Limit Equilibrium Analysis

Turfan 高昌故城 in silk-road China was an independent trading city in early seventeenth Century. Being ruled by a Chinese royal family, Turfan warmly hosted a Chinese monk, Xuánzang, 唐之玄奘, who traveled to India on foot for studying true Buddhism. This city had been destroyed by war, however, when the monk visited it again 17 years later on his way back to China.

Strong earthquake motion used to destroy many brick structures and killed many people. Figure 7.1 illustrates an example in Tokyo in which a brick tower of 12 storeys was destroyed in the middle. In those days there was no clear idea to design structures against earthquake effects. The same mechanism of collapse is still seen widely in many nonengineered structures in the world and the number of victims is substantial.

Fig. 7.1 Destroyed tower in Tokyo during 1923 Kanto earthquake (photograph from JSCE report)

The method of seismic coefficient (震度法) is the first measure to design facilities against earthquake effects. This method statically applies a force to a designed facility (pseudostatic or quasi-static method). The magnitude of this force is specified to be $K \times W$ in which K is called the seismic coefficient and W is the weight of the facility. Before this idea, there was no design method against earthquake effects. Since this method works easily with static calculation, it is still widely used. Figure 7.2 is an example of slope stability analysis.

A theoretical background of seismic coefficient lies in the *d'Alembert's* principle (ダランベールの原理) of mechanics. When a base of a structure has an acceleration of A, the effects of this shaking to the overlying structure is equivalent to a force of $(A/g)W$ in the opposite direction from the acceleration (Fig. 7.3); "g" stands for the gravity acceleration. Thus, the seismic coefficient of "K" appears to be equivalent to A/g.

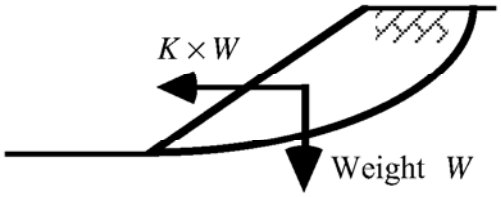

Fig. 7.2 Example of elementary seismic slope stability analysis

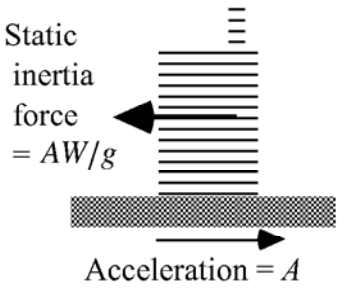

Fig. 7.3 d'Alembert's principle of mechanics.

The value of K today in Japan is 0.15–0.2 or greater. There is a variation in K, depending upon the local seismic activity, the importance of facilities, and the local geology or soil conditions.

The method of seismic coefficient is good because it is simple and the factor of safety can be calculated by the same way as the conventional static stress calculation. No advanced analysis is therein necessary. It made a great contribution to the improvement of seismic safety.

Fig. 7.4 A small hut that survived the 1994 Northridge earthquake

Problems lying in the seismic coefficient are as follows:

1. The real seismic force is cyclic, changing direction with time, and its duration time is limited. In contrast, the seismic coefficient method applies a force in a static manner. This seismic force overestimates the risk of earthquake failure.

2) At the time of 1994 Northridge earthquake near Los Angeles, the maximum horizontal acceleration of

1.8 G or possibly *1.9* G was recorded at Tarzana site (Fig. 6.25). Within tens of meters from the accelerometer here, a small hut did not suffer a damage (Fig. 7.4). Was this structure well designed against a horizontal static force as intense as 1.8 times its weight?

3) Thus, the relation between K and the maximum ground acceleration is not clear. 1.9 G acceleration does not mean $K = 1.9$. Study on seismic damage of quay walls led Noda et al. (1975) to propose

$$K = (A_{max}/g)^{1/3} / 3, \qquad (7.1)$$

in which A_{max} is the maximum horizontal acceleration (Sect. 12.3).

4) Many structures exhibit dynamic deformation during earthquake shaking. The intensity of shaking is normally greater in the upper portion than in the lower level. Therefore, a greater inertia force seems more appropriate near the top than near the bottom. This idea, called the modified seismic coefficient method, is already practiced in many situations; for example fill-type dams (Sect. 7.2).

The pioneer of seismic coefficient method of design in a modern sense was Prof. Toshikata Sano (1916 佐野利器博士; Fig. 7.5). He got an idea to apply horizontal force in design after his damage investigation on Great San Francisco earthquake (Sano, 1906). Since then, this method has been used at many places of the world. This method was further combined with the Coulomb active earth pressure theory (Appendix 1) to be the famous Mononobe-Okabe seismic (active) earth pressure theory (Sect. 12.5).

Fig. 7.5 Prof. T.Sano (from Memorial book of Dr. Toshikata Sano owned by Civil Engineering Library, University of Tokyo)

The idea of earthquake resistant design based on the seismic coefficient is written as

$$\text{Factor of safety} = \text{Resistance} / (\text{Static} + \text{seismic force}) > 1. \qquad (7.2)$$

Housner (1984) stated that the method of seismic coefficient was adopted in a design regulation in Italy after the 1908 Messina earthquake; Prof. M. Panetti proposed to design the first floor of a building with the seismic coefficient of 1/12, while upper stories with 1/8. The increased seismic coefficient in upper floors stands for the dynamic response of a building. This idea is equivalent with the modified seismic coefficient in Fig. 7.9.

Nakamura (2005) carried out dynamic centrifugal tests on distortion of a gravity retaining wall (refer to Fig. 12.25). He considered that A_{max} = 670 Gal of his seismic shaking was equivalent to the results of pseudostatic analysis in which $K=0.39$ made the factor of safety = 1. This is because A_{max} = 670 Gal triggered lateral translation of 1.5% of the wall height which seems to be equivalent with factor of safety = 1. Note that A_{max} = 670 Gal as substituted in (7.1) gives $K = 0.29$.

The method of seismic coefficient has drastically reduced the extent of damage and the number of casualties (victims) when it is "properly applied" to design and construction practice. It seems that this design principle was most effective for such brittle structures as the one in Fig. 7.1 which were made of bricks and a single big impact was enough to completely destroy them. See the highly brittle relationship between force and displacement in Fig. 7.6.

It seems that traditional (brick, adobe, and wooden) structures have had such a highly brittle nature (Fig.

7.6) that the resistance force drops significantly after the peak resistance. According to the method of seismic coefficient, seismic safety is achieved if the peak resistance is greater than the force (*static+seismic*). A catastrophic failure is possible, however, if the force level after the peak is lower than the static force. This was the case in the tower in Fig. 7.1. Another example of this type was Arg-e-Bam in Fig. 7.7. Being constructed before 500 BC, Arg-e-Bam was a miraculous ruin of an old fortress or citadel and a town where all the structures were made of adobe bricks. Upon the earthquake in 2003, however, those marvelous brick structures were destroyed instantaneously by strong shaking.

Recent developments of reinforced concrete and steel structures as well as geotechnical structures have changed the force–displacement relationship from a highly brittle one to a lightly brittle or ductile one. Since the force level after large displacement (deformation) is still held greater than the static force, a catastrophic failure is not so likely. In such a situation, it may not be necessary to maintain the factor of safety greater than 1 by making very elaborate design and spending money on high resistance. For more economical construction, the design requirement may be relaxed to some extent by allowing for the seismic factor of safety < 1 and still keeping the resultant displacement small enough (within an allowable extent). This is the aim of recent performance-based seismic design (Sect. 14.7).

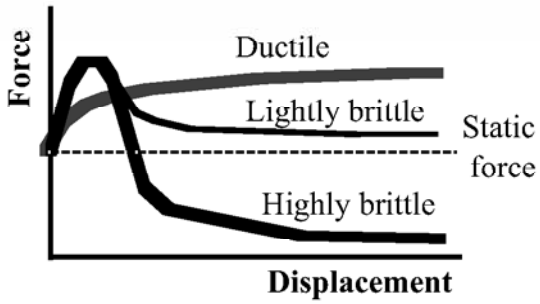

Fig. 7.6 Conceptual illustration of force-displacement relationships

Fig. 7.7 Damage of brittle structure (Arg-e-Bam Castle after 2003 Bam earthquake, Iran)

Since the performance-based design focuses mainly residual displacement, a large value of acceleration, A_{max}, is not necessarily taken seriously. In case the duration of A_{max} is short (Fig. 5.11), an equation of motion does not give large displacement. The nature of earthquake motion will be more reasonably considered by performance-based design than the conventional seismic coefficient method, which is influenced unduly by the magnitude of A_{max}. Since displacement analysis is conducted, on the other hand, the performance-based design requires more detailed understanding of soil behavior (more than strength) and hence more precise soil investigation.

Note that well-designed structures may be ductile during a strong earthquake, but furniture in rooms may fall down (highly brittle behavior) to injure residents.

The idea of uniform acceleration from the top to the bottom of a structure (Fig. 7.2) is not necessarily correct. It is often the case that the top exhibits a greater magnitude of motion than the bottom; amplification in flexible structures. One of the examples of this situation is found in an earth dam of which the trapezoidal shape increases the top motion significantly (see Sect. 6.13).

Figure 7.8 illustrates a situation in which a fill is subjected to an amplified shaking. The shear force between the top and the second blocks is given by $\tau_1 = m_1 A_1$. Since the acceleration varies in the vertical direction, the shear force at lower elevations is calculated by summation

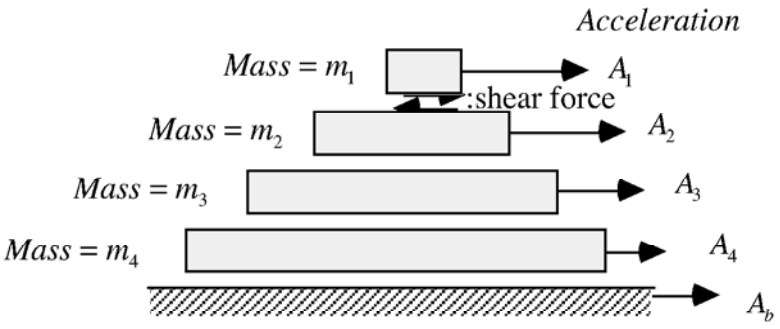

Fig. 7.8 Modified method of seismic coefficient

$$(\text{Shear force})_k = \sum_{i=1}^{k} m_i A_i = \sum_{i=1}^{k} (m_i g)\frac{A_i}{g},$$

where g stands for the gravitational acceleration, $m_i g$ is the weight of a block and $A_i / g = K_i$ is the seismic coefficient relevant for the ith block. It is evident that A_i is different from the base acceleration, A_b. The use of different values of $K_i = A_i / g$ in the vertical direction is called the modified method of seismic coefficient (修正震度法).

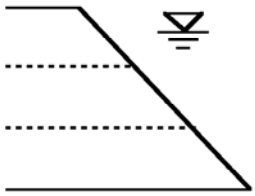

$K_1 = K_b \times 1.8$

$K_2 = K_b \times 1.4$

$K_3 = K_b \times 1.0$

K_b : seismic coefficient at base

Local seismic activity	K_b
High	0.18
Intermediate	0.16
Low	0.13

Fig. 7.9 Modified seismic coefficient in rockfill dam design

Figure 7.9 is an example idea of the modified seismic coefficients which is currently practiced for a seismic design of rockfill dams. Figure 7.10 is an example analysis on seismic limit equilibrium in which the critical slip plane is detected. In addition to this, consideration on a surface slip is necessary (Fig. 7.11).

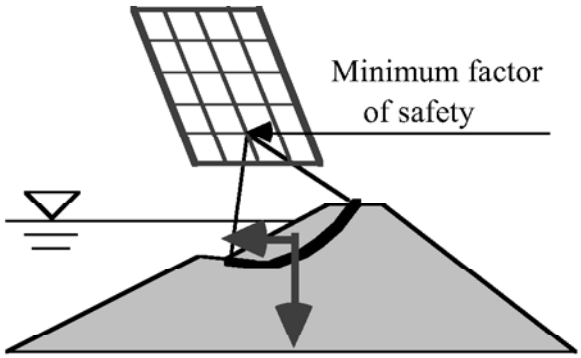

Fig. 7.10 Seismic analysis on earthdam by using limit equilibrium analysis

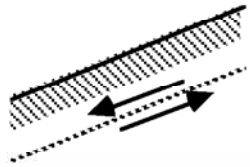

Fig. 7.11 Shallow slip failure

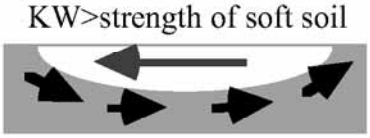

Fig. 7.12 Unrealistically predicted failure of level soft ground

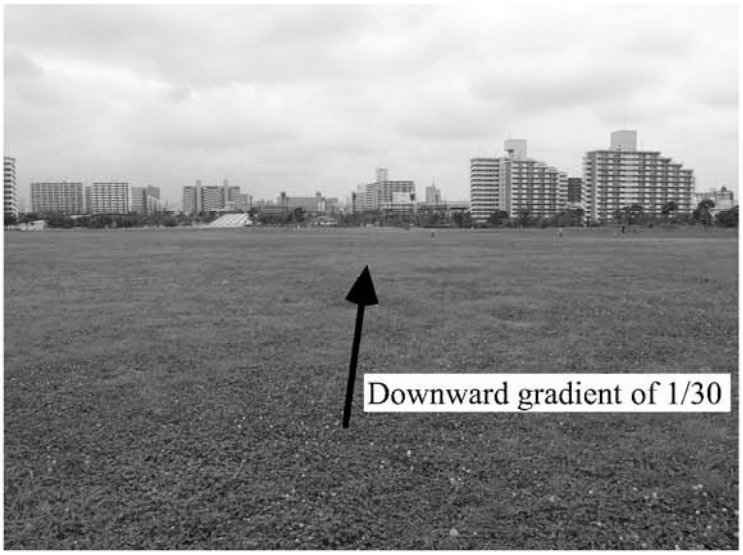

Fig. 7.13 Gentle slope of super river dike in Tokyo

The upstream slope of a fill dam is more gentle than the downstream slope. This is because the upstream soil is submerged in water and is heavier, generating a greater seismic inertia force. Moreover, the buoyancy force reduces the effective stress in the upstream side and makes the shear strength smaller. Possible development of excess pore water pressure and decrease in effective stress are important as well (Chap. 17).

One of the most ironical examples of the seismic coefficient method of analysis is that it predicts an overall failure of soft level subsoil (Fig. 7.12), although a level ground is unlikely to fail. This problem occurs because the method assumes a static one-way earthquake load despite that it is cyclic in reality. A symmetric loading in positive and negative directions does not accumulate deformation in a level subsoil. This shortcoming became a problem when a super river dike was designed in Tokyo (Fig. 7.13). The super rever dike has a slope gradient of merely 1/30 and buildings were placed on it. Hence, seismic stability of the dike slope was considered essentially important and a stability analysis was conducted. Since the dike was underlain by soft alluvial clay, the calculated factor of safety was less than unity in spite of the gentle slope. This case implies the importance of assessment of residual displacement by using, for example, the method in Sect. 12.1.

Conventionally, the horizontal motion has been attracting more attention than the vertical component. There are two reasons for this. First, any facility has some resistance against the vertical motion. The inertia force in the vertical downward direction increases the static force by, for instance, 20–50%. This increased load is often still within the static safety margin. Most failures in masonry structures are caused by the horizontal inertia force (Fig. 7.14).

Fig. 7.14 Collapse of adobe house in Bam, Iran, in 2003

When a slope stability is maintained by the frictional law (Fig. 7.15), the normal and the tangential reactions, N and S, are

$$N = (1 \pm K_v)W\cos\theta - K_h W \sin\theta \qquad \text{and}$$
$$S = (1 \pm K_v)W \sin\theta + K_h W \cos\theta ,$$

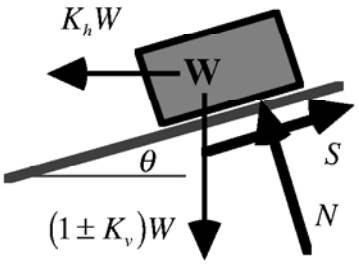

Fig. 7.15 Stability of block resting on frictional slope

where K_v and K_h stand for the vertical and horizontal seismic coefficients, respectively. Accordingly, the factor of safety, F_s, is derived as

$$F_s = \frac{\mu(1 \pm K_v - K_h \tan\theta)}{(1 \pm K_v)\tan\theta + K_h},$$

in which μ denotes the coefficient of friction. Although $1 \pm K_v$ does not vary substantially with K_v within a realistic range of variation, an increase in K_h directly reduces the factor of safety. Once the stability is lost, the block in Fig. 7.15 starts to slide down-slope and its displacement is (may be?) calculatcd by solving its cquation of motion.

In the example above, the increase in the normal force (N) directly increases the frictional resistance (μN). From the soil-mechanic viewpoint, this means that the slope is dry or under drained conditions. Conversely when the slope is undrained, which is more realistic under rapid loading, the increase in N is transferred to excess pore water pressure. Hence, the effective stress and consequently the frictional resistance do not change. The factor of safety is then given by

$$F_s = \frac{\mu N_{\text{initial}}}{S} = \frac{\mu}{(1 \pm K_v)\tan\theta + K_h}.$$

Again the horizontal inertia force, K_h, reduces the factor of safety.

Table 7.1 Maximum earthquake motion data (National Research Institute of Earth Science and Disaster Prevention, 1995)

Sites	Acceleration (Gal=cm/s^2) NS	EW	Up-Down
Kobe meteorological observatory [a]	818	617	332
Kobe port const. office	502	205	283
NTT Kobe building (B3F)	331	153	169
New Kobe station	530	267	344
Kobe port 8th pier [b]	683	394	334
Takatori station	635	553	175
Nishi Akashi station	397	381	319
Factory in Amagasaki	321	472	311
	Velocity (kine=cm/s)		
Univ. Kobe	55.1	31.0	33.2
Fukushima, Osaka	31.0	29.8	9.6
Chihaya-Akasaka	5.2	4.9	2.5

a Recorded at the top of a small hill.
b Recorded upon a quay structure, not on soil.

Empirically it is known that the vertical acceleration is weaker than the horizontal acceleration. Table 7.1 compares the maximum acceleration in vertical and horizontal directions recorded during the major earthquake in Kobe (1995). Generally, the vertical acceleration is half of the horizontal acceleration.

7.4 Direction of Seismic Inertia Force in Design

In many cases the seismic inertia force for design has been applied in the horizontal direction because the vertical acceleration in the observed records is weaker than the horizontal component. It might be interesting, however, to make a brief discussion on the appropriate direction of the design inertia force. It should be borne in mind that the following discussion is not very practical because the existing design values of seismic coefficient have been determined on the basis of the idea of horizontal inertia force, whether the idea is appropriate or not.

Figure 7.16 illustrates a situation in which a rigid body of weight = W is resting on a frictional slope. The inclination of the slope is θ, while the frictional angle between the slope floor and the rigid body is ϕ. Note that the inertia force of KW is inclined by an angle of α from the horizontal direction. It is aimed at in what follows to detect a particular α that minimizes the calculated factor of safety.

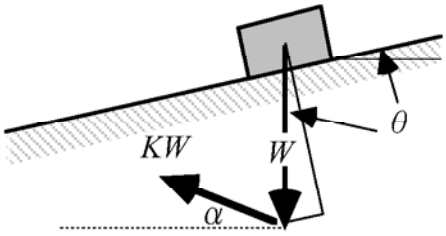

Fig. 7.16 Inclined direction of inertia force

The factor of safety, F_s, is calculated as the ratio of the frictional resistance and the driving force

$$F_s = \frac{(\text{Normal foce}) \times \tan\phi}{\text{Driving force}} = \frac{\{W\cos\theta - KW\sin(\theta+\alpha)\}\tan\phi}{W\sin\theta + KW\cos(\theta+\alpha)}$$
$$= \frac{\{\cos\theta - K\sin(\theta+\alpha)\}\tan\phi}{\sin\theta + K\cos(\theta+\alpha)}. \qquad (7.3)$$

The minimum factor of safety for varying α is detected by

$$\frac{\partial F_s}{\partial\alpha} = \frac{-K\cos(\theta+\alpha)\{\sin\theta + K\cos(\theta+\alpha)\} + K\sin(\theta+\alpha)\{\cos\theta - K\sin(\theta+\alpha)\}}{\{\sin\theta + K\cos(\theta+\alpha)\}^2}\tan\phi = 0.$$

Accordingly,

$$\sin\alpha = K \text{ and } \cos\alpha = \sqrt{1-K^2} \text{ for } K<1$$

as is practiced commonly.

The minimum factor of safety, $F_{s,\min}$, is obtained by substituting this special α in (7.3)

$$F_{s,\min} = \frac{\cos\theta - K\{\sin\theta\cos\alpha + \cos\theta\sin\alpha\}}{\sin\theta + K\{\cos\theta\cos\alpha - \sin\theta\sin\alpha\}}\tan\phi$$
$$= \frac{\cos\theta - K\left\{\sqrt{1-K^2}\sin\theta + K\cos\theta\right\}}{\sin\theta + K\left\{\sqrt{1-K^2}\cos\theta - K\sin\theta\right\}}\tan\phi$$
$$= \frac{\sqrt{1-K^2}\cos\theta - K\sin\theta}{\sqrt{1-K^2}\sin\theta + K\cos\theta}\tan\phi. \qquad (7.4)$$

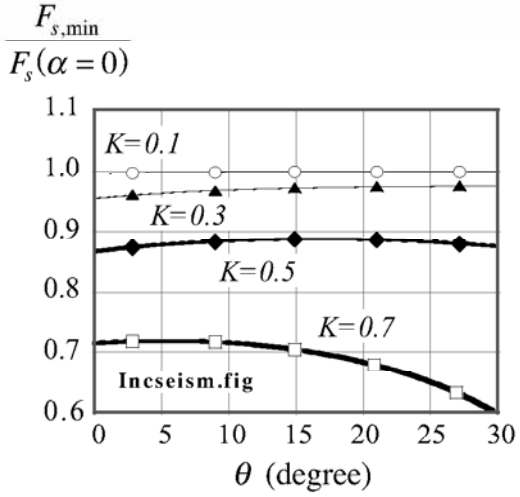

Fig. 7.17 Significance of inclined seismic inertia force

The conventional factor of safety, on the other hand, is derived by substituting $\alpha = 0$ in (7.3);

$$F_s = \frac{\cos\theta - K\sin\theta}{\sin\theta + K\cos\theta}\tan\phi. \qquad (7.5)$$

Finally, the significance of the inclined inertia force is illustrated by using the ratio of (7.4) and (7.5), see Fig. 7.17. It is found that the inclined direction of the inertia force reduces the calculated factor of safety to some extent. It is not very important, however, unless the employed seismic coefficient, K, is very large.

List of References in Chapter 7

Housner, G.W. (1984) Keynote lecture, 8th World Conf. Earthq. Eng., San Francisco, Post Conference Volume, pp. 25–39.

JSCE : Damage report on 1923 Kanto earthquake, Vol. 3.

Nakamura, S. (2005) Clarification of seismic behavior of gravity retaining wall by using centrifugal model tests and a proposal for rationalization of the seismic coefficient method, Proc. JSCE, Vol. 785/III-70, pp. 107–122 (in Japanese).

National Research Institute of Earth Science and Disaster Prevention (1995) Prompt report on strong-motion accelerograms No. 46 January 17, 1995 Southern Hyogo Prefecture, Feb.

Noda, S., Uwabe, T. and Chiba, T. (1975) Relation between seismic coefficient and ground acceleration for gravity quaywall , Report of the Port and Harbor Research Institute, Vol. 14, No. 4 (in Japanese).

Sano, T. (1906). Report on earthquake damage in California, USA 米國加州震災談, Journal of Architecture and Building Science 建築雜誌, Vol. 238, pp. 646–656 (in Japanese).

Sano, T. (1916) Aseismic design of buildings (I) 家屋耐震構造論 (上), No. 83A 甲, 震災豫防調査會 (Research Institute for Mitigation of Earthquake Disasters), p. 2 (in Japanese).